

Constraining barium isotope fractionation in the upper water column of the South China Sea

Zhimian Cao^{a,*}, Yating Li^a, Xinting Rao^a, Yang Yu^b, Ed C. Hathorne^b, Christopher Siebert^b, Minhan Dai^a, Martin Frank^b

^a State Key Laboratory of Marine Environmental Science & College of Ocean and Earth Sciences, Xiamen University, Xiang'an District, Xiamen 361102, China

^b GEOMAR Helmholtz Center for Ocean Research Kiel, Wischhofstrasse 1-3, Kiel 24148, Germany

* Corresponding author:

Dr. Zhimian Cao

Phone: +86-592-2186029

Fax: +86-592-2184101

E-mail: zmcao@xmu.edu.cn

13 Abstract

14 Enabled by the success in the determination of stable barium (Ba) isotopic compositions in seawater,
15 Ba isotopes have been suggested as a novel tool to study physical and biogeochemical processes in the
16 present and past ocean. However, a better understanding of the fractionation of Ba isotopes during
17 particle-seawater interactions is a prerequisite for such applications. In this study, we use an extensive
18 data set of concentrations and isotopic compositions of dissolved Ba (DBa and $\delta^{138}\text{Ba}_{\text{DBa}}$) and bulk
19 particulate Ba (pBa_{bulk} and $\delta^{138}\text{Ba}_{\text{pBa}_{\text{bulk}}}$) collected in the northern South China Sea (NSCS) to constrain
20 Ba isotope fractionation in the upper ocean. Seawater and suspended particle samples for Ba isotope
21 measurements were collected in January 2010 along a transect from the outer shelf to the lower slope.
22 The water column profiles reaching depths of 1000 m are characterized by a general decrease of
23 $\delta^{138}\text{Ba}_{\text{DBa}}$ and an increase of DBa with depth. However, $\delta^{138}\text{Ba}_{\text{DBa}}$ signatures are essentially constant at
24 $+0.6\text{‰}$ in the upper 150 m of the entire study area. The corresponding $\delta^{138}\text{Ba}_{\text{pBa}_{\text{bulk}}}$, which primarily
25 represents the isotopic compositions of oceanic or excess particulate Ba (pBa_{xs}), is consistently lower
26 than $\delta^{138}\text{Ba}_{\text{DBa}}$ but also constant at values of $+0.1$ to $+0.2\text{‰}$. This suggests that the same Ba isotope
27 fractionation process prevails above 150 m on the NSCS outer shelf and slope resulting in a constant in
28 situ fractionation factor of -0.5‰ . This value is consistent with previously reported values of -0.4 to
29 -0.5‰ in the upper 200 m of the open ocean and a lake. Moreover, we observe significant differences of
30 pBa_{xs} distributions from those of particulate calcium, particulate organic carbon and nitrogen, and
31 biogenic silica indicating that passive adsorption onto particles rather than active biological utilization is
32 most likely the primary process inducing Ba isotope fractionation in the upper NSCS. The constant
33 $\delta^{138}\text{Ba}_{\text{pBa}_{\text{bulk}}}$ signatures suggest that particulate Ba isotopes integrate reliable information during
34 transformation of DBa to pBa_{xs} and are thus a more robust proxy for total particle fluxes than pBa_{xs}
35 concentrations, which show variable values potentially affected by other processes (e.g., particle sinking

36 and/or zooplankton grazing) and thus reflects “snapshot” processes in the water column. We contend
37 that biological productivity plays only a subordinate role in regulating the surface Ba isotopic
38 composition of bulk suspended particles. The extent to which Ba isotopes may nevertheless be a reliable
39 proxy for present and past export productivity requires further analyses of the $\delta^{138}\text{Ba}$ signature of
40 specific Ba carriers such as barite throughout the water column and in the sediments.

1. INTRODUCTION

The element barium (Ba) has been widely used for tracing present and past biogeochemical processes in the ocean. Due to its systematic spatial variations and distinct endmembers, dissolved Ba (DBa) is a useful tracer of water masses and ocean circulation (Hall and Chan, 2004; Jacquet et al., 2016) and of mixing between river waters and seawater (Guay and Falkner, 1998; Weldeab et al., 2007). Particle adsorption or crystallization largely controls the formation of excess particulate Ba (pBa_{xs} , the fraction of oceanic Ba in bulk particles that is not lithogenic) in the uppermost water column (Dehairs et al., 1980). During particle sinking and subsequent decomposition at depth, a fraction of the regenerated Ba precipitates as microcrystalline barite ($BaSO_4$) in oversaturated microenvironments, which frequently leads to a mesopelagic pBa_{xs} maximum (Jacquet et al., 2008, and references therein). In the deep ocean, barite dissolution and large scale circulation mainly control the distribution of DBa.

Since barite formation in the mesopelagic zone is largely associated with organic matter decomposition, pBa_{xs} concentrations show an overall positive linear relationship with oxygen utilization rate and are thus used to estimate carbon remineralization in intermediate waters (Dehairs et al., 1997; Lemaitre et al., 2018). Because elevated carbon export and remineralization generally increase pBa_{xs} or barite concentrations in the water column, its accumulation in sediments provides a direct link to paleoproductivity (Carter et al., 2020, and references therein). Therefore, pBa_{xs} represents a potentially sensitive tracer of carbon cycling in both the present and past ocean.

However, several problems fundamental to understanding biogeochemical Ba cycling remain elusive. While the nutrient-like distribution of DBa appears mainly controlled by barite formation and dissolution, the two to three orders of magnitude higher concentrations of DBa with respect to pBa_{xs} complicate the quantification of processes inducing the non-conservative behavior of the dissolved phase (Jacquet et al., 2007). The actual mechanisms resulting in a mesopelagic pBa_{xs} maximum in the

64 water column are still under debate (Ganeshram et al., 2003; González-Muñoz et al., 2003; Bernstein
65 and Byrne, 2004; Martinez-Ruiz et al., 2018), which limits the application of the sedimentary pBa_{xs}
66 proxy (McManus et al., 1998). Possible lateral inputs from shelf environments further complicate its
67 application (Cardinal et al., 2001).

68 Recent analyses of stable isotopic compositions of dissolved Ba in seawater reveal measurable
69 variations responding to relevant physical and biogeochemical processes controlling the oceanic Ba
70 cycle. While the Ba isotopic compositions are essentially constant between the surface and 100-200 m
71 depth in the open ocean (Horner et al., 2015; Bates et al., 2017; Hsieh and Henderson, 2017;
72 Bridgestock et al., 2018; Hemsing et al., 2018; Geyman et al., 2019) and the offshore area of marginal
73 seas beyond the river influence (Cao et al., 2020), they are significantly heavier than those in the deeper
74 waters documenting a nutrient-like isotope distribution. This gradient from the surface to 500-600 m
75 depth is generally attributed to barite cycling (Horner et al., 2015; Bridgestock et al., 2018), while Cao et
76 al. (2016, 2020) suggested that the constant and distinctly heavy signal of dissolved Ba isotopes in the
77 upper 100 m is primarily induced by particle adsorption. This is supported by one profile in the South
78 Atlantic (Horner et al., 2017) and one in the South China Sea (SCS; Cao et al., 2020), both of which
79 showed consistently lighter Ba isotopic signatures of suspended particles in the upper water column. Ba
80 isotopic compositions of sinking particles in both the water column (via model estimation; Bridgestock
81 et al., 2018) and the sediment (via field measurements; Bridgestock et al., 2018, 2019; Nielsen et al.,
82 2018; Crockford et al., 2019) are also systematically lighter than those of seawater.

83 Although previous studies clearly indicated Ba isotope fractionation in the upper ocean,
84 comprehensive analyses of dissolved and particulate Ba isotopic compositions are needed, in order to
85 better understand the dynamics and fractionation of Ba isotopes and their links to ocean biogeochemistry.
86 In this study, we determined the Ba isotopic distribution of seawater DBa ($\delta^{138}\text{Ba}_{\text{DBa}}$) and of bulk

87 particulate Ba (pBa_{bulk}) in suspended particles ($\delta^{138}Ba_{pBa_{bulk}}$) in the northern SCS (NSCS) extending
88 from the outer shelf to the lower slope. Using these samples we systematically investigate coupled and
89 concurrent dissolved and particulate $\delta^{138}Ba$ signatures for the first time and quantify the Ba isotope
90 fractionation associated with the transformation of DBa to pBa_{xs} . In addition, the potential mechanisms
91 controlling this fractionation are explored by comparing the distribution of Ba with that of biogenic
92 elements including carbon and major nutrients in both the dissolved and particulate phases.

93 **2. MATERIALS AND METHODS**

94 **2.1. Study area**

95 The SCS is the largest marginal sea of the Pacific Ocean, covering a surface area of 3.5×10^6 km². The
96 East Asian Monsoon prevails in the SCS resulting in a seasonal reversal of surface circulation from a
97 cyclonic gyre in winter to an anticyclonic gyre in summer (Fig. 1). Owing to inputs from some of the
98 world's largest rivers (e.g., the Mekong River and the Pearl River; Grosse et al., 2010; Cao et al., 2011;
99 Fig. 1) and the influence of strong upwelling and vertical mixing (Chao et al., 1996; Wong et al., 2007),
100 the upper water column of the SCS receives elevated supplies of nutrients leading to a higher biological
101 productivity than in the adjacent western North Pacific (wNP; Liu et al., 2002; Du et al., 2013). The SCS
102 and the wNP exchange waters via the 2200 m deep Luzon Strait, displaying a “sandwich-like” structure
103 comprising a net inflow from the Pacific both near the surface (i.e., Kuroshio Branch Water, KBW; Fig.
104 1) and in deep layers, and a net outflow from the SCS at intermediate depths (Cao and Dai, 2011, and
105 references therein). In terms of mass balance, the rapid replenishment of the SCS deep waters from the
106 wNP, on the order of 30 years, is maintained by the rapid ventilation above 1500 m and persistent net
107 outflow to the Pacific between 500 and 1500 m water depth (Chao et al., 1996; Gan et al., 2016).

108 **2.2. Sampling and analyses**

109 *2.2.1. Sampling*

110 In January 2010, seawater and suspended particle samples were collected with Niskin bottles attached
111 to a rosette sampler at stations A5, A2, A1, A10, and S504 extending from the outer shelf to the lower
112 slope of the NSCS (the bottom depths of these stations are ~100 m, ~400 m, ~850 m, ~2800 m and
113 ~3100 m; Fig. 1). Seawater samples were obtained by filtering 250-500 mL of seawater through 0.45
114 μm nitrocellulose acetate filters into acid pre-cleaned polyethylene bottles. DBa and $\delta^{138}\text{Ba}_{\text{DBa}}$ samples
115 were subsequently acidified to pH~2 with distilled concentrated HCl (0.1% v/v) and stored at room
116 temperature in the dark. Suspended particle samples for pBa_{bulk} (or pBa_{xs}), $\delta^{138}\text{Ba}_{\text{pBa}_{\text{bulk}}}$, and particulate
117 aluminum and calcium (pAl and pCa) analyses were obtained by filtering 2-5 L of seawater through 0.4
118 μm polycarbonate membrane filters. The filters were dried at 50°C overnight and stored in
119 polycarbonate dishes for analysis at Xiamen University.

120 2.2.2. Ba concentration analyses

121 DBa concentrations in seawater were analyzed using isotope dilution ICP-MS (Klinkhammer and
122 Chan, 1990; Freydier et al., 1995). Briefly, ~200 μL of seawater was accurately weighed and mixed with
123 defined amounts of the ^{135}Ba -enriched single spike to obtain a $^{138}\text{Ba}/^{135}\text{Ba}$ ratio between 0.7 and 1. After
124 dilution, $^{138}\text{Ba}/^{135}\text{Ba}$ ratios were measured with an Agilent 7700x ICP-MS using bracketing analyses of a
125 natural Ba standard solution to correct for mass bias. Repeated measurements of two seawater reference
126 materials (CASS-5 and NASS-6, National Research Council of Canada) resulted in a precision of $\pm 3\%$
127 (2 standard deviation (2SD), $n=5$, respectively).

128 The suspended particle samples were digested via reaction with concentrated acids (3 mL HCl+2 mL
129 HNO_3 +1mL HF) at 90°C overnight (Cardinal et al., 2001). Particulate Ba, as well as pAl and pCa, were
130 analyzed by measuring Ba, Al, and Ca in the digested solution with an Agilent 7700x ICP-MS. pBa_{xs}
131 concentrations deposited on the filter membranes were calculated by the excess above lithogenic Ba/Al
132 ratios ($[\text{pBa}_{\text{xs}}]=[\text{Ba}]-[\text{Al}]\times\text{Ba}/\text{Al}_{\text{litho}}$). [Ba] and [Al] denote Ba and Al concentrations in the digested

133 solution. For the Ba/Al_{litho} molar ratio, we selected an average value of 0.00135 for the upper continental
 134 crust (Taylor and McLennan, 1985), which is widely used to calibrate the lithogenic Ba in both
 135 suspended particles in the water column (e.g., Cardinal et al., 2001; Jacquet et al., 2015) and sinking
 136 particles in the sediments (e.g., François et al., 1995; Winckler et al., 2016). The results showed that the
 137 oceanic pBa_{xs} in nearly all suspended particle samples contributes to >90% of the total particulate Ba
 138 content, whereas the highest portion of lithogenic Ba is 27% at 75 m depth at station A5 (Table 3), but
 139 the very low pBa_{bulk} concentration of this sample did not allow for a precise $\delta^{138}\text{Ba}$ measurement. If the
 140 highest Ba/Al_{litho} molar ratio ever reported (0.00197; Taylor and McLennan, 1985) is used, this portion
 141 would reach 40%.

142 2.2.3. Ba isotope analyses

143 Ba isotopic compositions were measured using a double spike technique and are reported in ‰
 144 deviations from the international Ba standard NIST SRM 3104a (Ba(NO₃)₂, Lot: 070222;
 145 $\delta^{138}\text{Ba}_{\text{NIST}} = [(^{138}\text{Ba}/^{134}\text{Ba})_{\text{sample}} / (^{138}\text{Ba}/^{134}\text{Ba})_{\text{standard}} - 1] \times 1000$). A ¹³⁰Ba-¹³⁵Ba double spike was prepared
 146 from ¹³⁰BaCO₃ and ¹³⁵BaCO₃ (ORNL enriched to 35.8 and 93.4%, respectively). We did not measure
 147 the actual ¹³⁸Ba signal in our method because the dynamic range of the used Nu Instruments HR MC-
 148 ICP-MS at Xiamen University is not large enough to analyze ¹³⁸Ba (natural abundance of 71.70%)
 149 simultaneously with the remaining Ba masses and maintain sufficient counting statistics. We only report
 150 $\delta^{138}\text{Ba}_{\text{NIST}}$ values in this contribution (Figs. 3, 4, and 6; Supplementary Fig. 1) by multiplying $\delta^{137}\text{Ba}_{\text{NIST}}$
 151 by 1.33 assuming mass-dependent fractionation (Horner et al., 2015).

152 The ¹³⁰Ba-¹³⁵Ba double spike was added to seawater and solutions of digested suspended particle
 153 samples and allowed to equilibrate overnight. After evaporation to dryness and redissolution, Ba was
 154 purified from the sample matrix using cation-exchange chromatography with an average yield of 90%
 155 for the entire chemical preparation procedure. Note that for seawater samples an additional cation-

exchange column step was applied to ensure complete removal of all matrix elements to avoid anomalously heavy $\delta^{138}\text{Ba}_{\text{NIST}}$ signatures. However, this matrix effect can be significantly attenuated by tuning for an increased Normalized Ar Index (NAI; an index of plasma temperature) during MC-ICP-MS measurements (Yu et al., 2020). By chemically treating 40 mL of Milli-Q water the same way as the seawater samples, the total procedural Ba blank was established to be <0.2 ng, which is $<0.1\%$ of the Ba introduced into the MC-ICP-MS for each sample solution (2 mL solution with a Ba concentration of ~ 100 ppb). By filtering 4 L of Milli-Q water onboard and digestion in the same way as the particle samples, the Ba blank for filters was on average $<1\%$ of the Ba processed in the samples, with the highest values of 2-3% in only two samples. Such low blank levels support negligible impact on Ba isotopic compositions of both seawater and suspended particle samples.

The purified sample solutions were introduced as a dry aerosol into the plasma using a DSN-100 desolvator (Nu Instruments) equipped with a PFA nebulizer with an uptake rate of $\sim 75 \mu\text{L min}^{-1}$. For data reduction the geometrical procedure described in Siebert et al. (2001) was used and each spiked sample measurement of $\delta^{137}\text{Ba}$ was normalized to two “bracketing” spiked standard measurements. Each sample solution was analyzed two to three times (except four particle samples because of too low Ba content in digested solutions) in a single measurement session resulting in sample reproducibilities between ± 0.01 and $\pm 0.15\%$ (2SD; Tables 1 and 2). Repeated measurements of four in-house standards between April 2017 and December 2019 gave average $\delta^{137}\text{Ba}_{\text{NIST}}$ values of $-0.04 \pm 0.03\%$ (2SD, $n=14$; $\text{Ba}(\text{NO}_3)_2$ standard solution, Inorganic Ventures), $+0.08 \pm 0.04\%$ (2SD, $n=22$; IAEA-SO-5, BaSO_4 , IAEA), $+0.06 \pm 0.04\%$ (2SD, $n=20$; IAEA-SO-6, BaSO_4 , IAEA), and $+0.28 \pm 0.05\%$ (2SD, $n=12$; seawater collected at 500 m depth in the NSCS basin). The long-term external 2SD reproducibility was thus $\pm 0.05\%$ for $\delta^{137}\text{Ba}_{\text{NIST}}$ and $\pm 0.06\%$ for $\delta^{138}\text{Ba}_{\text{NIST}}$, respectively. The latter represents the uncertainty of field data provided in this study (Figs. 3, 4, and 6; Supplementary Fig. 1).

179 Our measurements of two artificially fractionated Ba isotope standards yield $\delta^{137}\text{Ba}_{\text{NIST}}$ of $-1.14 \pm 0.09\text{‰}$
 180 (2SD, n=4) for BaBe12 and of $-0.62 \pm 0.07\text{‰}$ (2SD, n=7) for BaBe27, both of which are within
 181 analytical error indistinguishable from the values (BaBe12: $-1.16 \pm 0.05\text{‰}$ and BaBe27: $-0.62 \pm 0.05\text{‰}$)
 182 reported by van Zuilen et al. (2016b). We also analyzed the GEOTRACES SAFe seawater reference
 183 material. Our $\delta^{138}\text{Ba}_{\text{NIST}}$ data (surface: $+0.62 \pm 0.04\text{‰}$, 2SD, n=2 and deep: $+0.28 \pm 0.09\text{‰}$, 2SD, n=2) are
 184 identical to those reported by three other labs (surface: $+0.62 \pm 0.02\text{‰}$ and deep: $+0.27 \pm 0.02\text{‰}$, Hsieh
 185 and Henderson, 2017; surface: $+0.63 \pm 0.04\text{‰}$ and deep: $+0.32 \pm 0.03\text{‰}$, Geyman et al., 2019; surface:
 186 $+0.64 \pm 0.08\text{‰}$ and deep: $+0.29 \pm 0.02\text{‰}$, Cao et al., 2020) and thus lend additional support to the validity
 187 of $\delta^{138}\text{Ba}_{\text{NIST}}$ values obtained in this study. Our $\delta^{138}\text{Ba}_{\text{DBa}}$ of all seawater samples varies within a range
 188 of $+0.3$ - 0.6‰ in the upper 1000 m of the NSCS and matches previous observations in the open ocean
 189 water column (Horner et al., 2015; Bates et al., 2017; Hsieh and Henderson, 2017; Bridgestock et al.,
 190 2018; Hemsing et al., 2018; Geyman et al., 2019).

191 A lithogenic Ba content of $<6\%$ was deduced from Al concentrations in the digested solution of
 192 nearly all suspended particle samples (Table 3) indicating that Ba in these particles is dominantly of
 193 oceanic origin. The corresponding $\delta^{138}\text{Ba}_{\text{pBabulk}}$ thus reflects the isotopic composition of oceanic pBa_{xs}
 194 ($\delta^{138}\text{Ba}_{\text{pBaxs}}$) without lithogenic corrections. Three exceptions are samples from 25 and 75 m depths at
 195 station A5 and the sample from 125 m depth at station A2, where lithogenic Ba accounts for ~ 18 , ~ 27 ,
 196 and $\sim 16\%$ of total particulate Ba content. Natural lithogenic $\delta^{138}\text{Ba}_{\text{NIST}}$ values around 0‰ have been
 197 reported for both marine (-0.1 to 0‰ ; Bridgestock et al., 2018) and river sediments (-0.05 to $+0.04\text{‰}$;
 198 Nan et al., 2018) and for the upper continental crust (on average $0.00 \pm 0.04\text{‰}$; Nan et al., 2018).
 199 Assuming $\delta^{138}\text{Ba}_{\text{NIST}}$ of -0.10‰ and $+0.05\text{‰}$ (lower and upper limits) for lithogenic Ba and of $+0.13\text{‰}$
 200 for oceanic pBa_{xs} (the average $\delta^{138}\text{Ba}_{\text{pBabulk}}$ of all other suspended particle samples in this study),
 201 $\delta^{138}\text{Ba}_{\text{pBabulk}}$ values of samples at 25 m depth at station A5 and 125 m depth at station A2 are both

202 estimated to be +0.09 and +0.12‰, which are, respectively, lighter than and/or identical to our measured
203 $\delta^{138}\text{Ba}_{\text{pBabulk}}$ of +0.19±0.05 and +0.05±0.10‰ (Table 2). The estimate of lithogenic corrections and the
204 measurement are also within error indistinguishable from the average $\delta^{138}\text{Ba}_{\text{pBaxs}}$ signature. We are
205 therefore confident that the $\delta^{138}\text{Ba}_{\text{pBabulk}}$ data reported in this study reliably represent the oceanic
206 $\delta^{138}\text{Ba}_{\text{pBaxs}}$.

207 3. RESULTS

208 3.1. Hydrography

209 During the sampling period in winter, the entire water column at station A5 on the NSCS outer shelf
210 was well mixed as demonstrated by the nearly uniform potential temperature (PT), salinity, and density
211 (σ_0) values (Fig. 2). The water column in the upper 100 m ($\sigma_0 < 24.5$) at stations on the NSCS slope
212 generally displays increasing salinity and decreasing PT with increasing σ_0 levels, suggesting
213 stratification with the surface mixed layer above depths of 50-80 m ($\sigma_0 < 23.5$ for stations A2 and A1 and
214 $\sigma_0 < 22.8$ for stations A10 and S504; Fig. 3b-3e). Salinities in the very surface waters at these locations
215 are higher than 33.5 showing no input from the Pearl River plume (salinity < 33.0 ; Cao et al., 2011) in
216 this dry season. These values gradually decrease from 34.4 at station A5 to 34.1 at stations A2 and A1 to
217 33.8 at stations A10 and S504 (Fig. 2). Such a gradient suggests possible influence of more saline KBW
218 (salinity > 34.5) on the outer shelf, which is weakened on the upper and middle slope and is negligible on
219 the lower slope. However, the highest surface salinity observed at station A5 is likely derived from the
220 deeper interior of the SCS, given that the strong upwelling and vertical mixing prevails in winter in the
221 SCS (Cao et al., 2012, and references therein). The relatively fresh surface waters at stations A10 and
222 S504 are most likely attributable to the net precipitation over the SCS basin. A salinity maximum
223 of > 34.67 is observed at 100-140 m depth ($\sigma_0 \sim 24.5$ -24.9) at stations A2 and A1, while a slightly weaker
224 and deeper one of > 34.62 is observed at 150-170 m depth ($\sigma_0 \sim 25.2$) at stations A10 and S504. These

225 salinity maxima result from the advection of North Pacific Tropical Water sourced in the subtropical
226 region (Suga et al. 2000), which exerts more influence at the former two stations. T-S distribution
227 patterns below 150 m ($\sigma_0 > 25.0$) are nearly identical at stations A2, A1, A10, and S504 suggesting that
228 the deeper water column up to 1000 m is occupied by uniform water masses on the NSCS slope. A
229 salinity minimum of < 34.42 is observed in the intermediate waters near 350-400 m water depth
230 ($\sigma_0 \sim 26.5$ -26.6) at the latter three stations, which is attributed to the advection of North Pacific
231 Intermediate Water sourced in the subpolar region (You, 2003) (Fig. 2).

232 **3.2. Distributions of $\delta^{138}\text{Ba}_{\text{DBa}}$ and $\delta^{138}\text{Ba}_{\text{pBa}_{\text{bulk}}}$ in the upper 150 m**

233 DBa concentrations in the very surface waters are homogenous on the NSCS outer shelf and slope
234 with an average value of $34.5 \pm 1.1 \text{ nmol kg}^{-1}$ (1SD, $n=5$). Although the vertical profiles of DBa in the
235 upper 150 m apparently display variable distributions between stations, the largest difference at each
236 station of 1.2 to 3.6 nmol kg^{-1} is just outside analytical uncertainty (Fig. 3f-3j; Table 1). The dissolved
237 $\delta^{138}\text{Ba}_{\text{NIST}}$ of $+0.60 \pm 0.02\text{‰}$ (1SD, $n=5$) in the very surface waters is also essentially homogenous
238 between the five sampling stations. All $\delta^{138}\text{Ba}_{\text{DBa}}$ values are within analytical uncertainty identical to
239 $+0.60\text{‰}$ from the surface to near-bottom or 150 m water depth, except that the $\delta^{138}\text{Ba}_{\text{DBa}}$ signature in
240 waters near the 150 m depth at station S504 ($+0.53\text{‰}$) is slightly lighter (Fig. 3k-3o; Table 1).

241 pBa_{bulk} concentrations in suspended particles in the upper 150 m range between 200 and 1100 pmol
242 kg^{-1} , which are overall more than one order of magnitude lower than the corresponding DBa
243 concentrations (Fig. 3f-3j; Tables 1 and 2). The vertical profiles of pBa_{bulk} are variable. At stations A5
244 on the NSCS outer shelf, pBa_{bulk} concentrations at 25 m depth are higher than those at 75 m depth, even
245 though the latter has larger fraction of lithogenic Ba. On the NSCS slope, however, pBa_{bulk} generally
246 increases from the surface mixed layer to 150 m depth at stations A1, A10, and S504, whereas a marked
247 peak is observed at the 75 m depth at station A1 (Fig. 3h-3j). In contrast to pBa_{bulk} concentrations, the

248 $\delta^{138}\text{Ba}_{\text{pBa bulk}}$ signatures are nearly constant at +0.1 to +0.2‰ throughout the upper 150 m water column
249 of the entire study area, while $\delta^{138}\text{Ba}_{\text{pBa bulk}}$ near the 150 m depth at stations A1 and S504 (+0.04±0.07
250 and +0.06±0.06‰, respectively) is slightly lighter than that in the top 25 m of the two stations (on
251 average +0.20±0.02‰, 1SD, n=4) (Fig. 3k-3o; Table 2).

252 **3.3. Distributions of $\delta^{138}\text{Ba}_{\text{DBa}}$ at stations A1, A10, and S504 in the upper 1000 m**

253 The vertical distributions of $\delta^{138}\text{Ba}_{\text{DBa}}$ generally mirror those of DBa in the upper 1000 m at stations
254 A1, A10, and S504. Moreover, both DBa concentrations and $\delta^{138}\text{Ba}_{\text{DBa}}$ signatures at any depth are
255 comparable between the three stations (Fig. 4) suggesting the major control of water mass mixing on the
256 NSCS slope. Below 150 m DBa concentrations increase rapidly down to the 1000 m water depth at a
257 value around 100 nmol kg⁻¹ (Fig. 4a; Table 1). Correspondingly, $\delta^{138}\text{Ba}_{\text{DBa}}$ values decrease linearly from
258 the 150 to 800-1000 m water depth at a value of +0.3‰ (Fig. 4b; Table 1), which agrees well with data
259 obtained in the deep waters below 1000 m of the NSCS basin (Cao et al., 2020).

260 **4. DISCUSSION**

261 Our results show significant fractionation between particulate and dissolved Ba isotopes in the upper
262 150 m of the NSCS. While the isotopic compositions of both phases are nearly invariant within the
263 upper water column, the pBa_{bulk} concentrations vary significantly and are often decoupled from DBa.
264 Deeper seawater samples show a typical nutrient-like distribution of DBa and $\delta^{138}\text{Ba}_{\text{DBa}}$ as observed in
265 previous studies (Horner et al., 2015; Cao et al., 2020; Bates et al., 2017; Hsieh and Henderson, 2017;
266 Bridgestock et al., 2018; Hemsing et al., 2018; Geyman et al., 2019). These features allow us to discuss
267 the mechanisms controlling Ba behavior in the NSCS.

268 **4.1. Comparison between pBa_{xs} and other particulate matter**

269 The average pBa_{xs} concentration of 560 pmol kg⁻¹ is within the range of 10-600 pmol kg⁻¹ generally
270 observed in the upper open ocean (Dehairs et al., 1997; Jeandel et al., 2000; Bishop and Wood, 2008;

Dehairs et al., 2008; Jacquet et al., 2008). However, the observed absolute range in the NSCS is significantly larger between 170 and 1050 pmol kg⁻¹ (Table 3). Comparably high pBa_{xs} concentrations near 1700 pmol kg⁻¹ were observed at 50 m in the Western Mediterranean Sea (van Beek et al., 2009) and extremely high values were observed in the Southern Ocean, e.g., 7512-9112 pmol kg⁻¹ in the upper 100 m of the Polar Front Zone (Dehairs et al., 1997) and 1354-5930 pmol kg⁻¹ at the 50 m depth in the Kerguelen Island area (Jacquet et al., 2008). Jacquet et al. (2015) stated that such high values are not unusual and likely associated with phytoplankton-derived particles. We contend that biological influence may also be responsible for some relatively high pBa_{xs} in our samples, which we will argue below is not directly produced via active intracellular uptake of Ba by living phytoplankton.

In order to assess the role of various particulate phases in pBa_{xs} accumulation we estimate the influence of lithogenic minerals and compare the observed pBa_{xs} to proxies for biogenic particulate matter. The observed pAl concentrations of 5-40 nmol kg⁻¹ (with three exceptions of >45 nmol kg⁻¹; Table 3) are comparable to or slightly higher than those observed in the open ocean such as the North Pacific (Dehairs et al., 2008), the tropical North Atlantic (Jeandel et al., 2000), and the Southern Ocean (Jacquet et al., 2011), which suggests an overall very small fraction of lithogenic components in suspended particles in the upper water column of the NSCS slope during the sampling period.

pCa (an approximation of particulate inorganic carbon, PIC) concentrations collected for this study in January range from 80 to 300 nmol kg⁻¹ (Table 3), which are comparable to or slightly higher than the PIC concentrations collected in the upper 150 m of the NSCS basin in September (Cao et al., 2009). This is expected given that calcium carbonate is the dominant component of PIC in the ocean and the biological production in the NSCS is generally higher in winter than in summer (Chen, 2005). The vertical profiles of particulate organic carbon and nitrogen (POC and PON; data were previously published in Cai et al. (2015)) display similar distribution patterns at all sampling stations with PON

consistently lower than POC (Fig. 5c, 5g, 5k, 5o, and 5s). The average POC/PON ratio of 6.9 ± 1.1 agrees with the Redfield ratio (Redfield et al., 1963) confirming their origin from phytoplankton photosynthesis. Biogenic silica (BSi) concentrations are overall comparable to those of PON (0.08-0.56 versus 0.12-0.71 $\mu\text{mol L}^{-1}$; Table 3) suggesting enhanced diatom productivity in winter on the NSCS outer shelf and slope (Chen, 2005).

The vertical distributions of pBa_{xs} clearly do not follow those of biogenic particles including pCa, POC, PON, and BSi. All these phytoplankton-derived particles, except for BSi at station A10, display high concentrations from the very surface to 50-75 m water depth, which are marked by high concentrations of chlorophyll a (Chl-a; data were previously published in Chen et al. (2015)) (Fig. 5). The lack of co-variation of pBa_{xs} implies that the primary process controlling the formation of excess particulate Ba is different from those for biogenic particulate C, N, and Si in the upper NSCS. The apparently unsystematic distributions of pBa_{xs} have also been observed in other oceanic environments, e.g., the Southern Ocean (Jacquet et al., 2011), the North Atlantic Ocean (Lemaitre et al., 2018), and the Mediterranean Sea (van Beek et al., 2009).

4.2. Mechanisms controlling the dynamics of Ba isotopes in the NSCS

4.2.1. Vertical supply of DBa from depth and Ba isotope fractionation in the upper 150 m

The upper 1000 m of the water column in the NSCS consists of multiple water masses as suggested by the T-S diagram showing at least three different linear relationships (Fig. 2), and the dissolved Ba data display a good linear relationship between $1/\text{DBa}$ and $\delta^{138}\text{Ba}_{\text{DBa}}$ ($r^2=0.93$, $n=37$; Fig. 6). While the deep waters around 800-1000 m have the lowest $\delta^{138}\text{Ba}_{\text{DBa}}$ values and highest DBa concentrations, a systematic and continuous upward increase of $\delta^{138}\text{Ba}_{\text{DBa}}$ accompanied by a decrease of DBa occurs up to the depth of the (sub)surface waters at and above 150 m (Fig. 6), suggesting a major control of

316 upwelling or diapycnal mixing (e.g., vertical diffusion) between water masses at different depths in the
317 interior of the NSCS (Chao et al., 1996; Tian et al., 2009).

318 Although the KBW may have influenced the surface waters on the outer shelf and upper slope, no
319 evidence of this can be found in the Ba isotopic compositions, which show the same surface $\delta^{138}\text{Ba}_{\text{DBa}}$
320 values as in the lower slope (this study) and deep basin (Cao et al., 2020) of the NSCS. Surface DBa
321 concentrations around $34.5 \text{ nmol kg}^{-1}$, which are comparable to those in the open Pacific (Bacon and
322 Edmond, 1972; Monnin et al., 1999; Esser and Volpe, 2002; Geyman et al., 2019), further suggest
323 negligible influence from the river discharge highly enriched in Ba (Guay and Falkner, 1998; Cao et al.,
324 2020). In addition, potential effects on Ba isotopic compositions during particle remineralization may be
325 too small to be detected outside analytical uncertainty of the $\delta^{138}\text{Ba}_{\text{DBa}}$ signatures due to the
326 overwhelmingly large dissolved pool, and thus cannot be distinguished from the dominant control of
327 water mass mixing (Bates et al., 2017).

328 We therefore infer that the primary DBa source in the upper NSCS during the sampling period was
329 vertical mixing from the underlying waters below 150 m, whereas contributions of processes such as
330 horizontal mixing and remineralization are probably negligible at these depths. Significant fractionation
331 of Ba isotopes with respect to its source waters from depth is thus indicated by the heavy $\delta^{138}\text{Ba}_{\text{DBa}}$
332 values and correspondingly light $\delta^{138}\text{Ba}_{\text{pBa bulk}}$ values in the upper 150 m (Fig. 6).

333 4.2.2. Fractionation induced by particle adsorption rather than biological utilization

334 On the basis of the observed decoupling of Ba from the major nutrients in the East China Sea and in
335 the NSCS basin, Cao et al. (2016, 2020) inferred that Ba isotope fractionation in the upper water column
336 is primarily induced by preferential adsorption of the lighter Ba isotopes onto particles rather than by
337 biological utilization. Such a decoupling also occurs on the NSCS outer shelf and slope confirming these
338 earlier results. While concentrations of phosphate (PO_4), nitrate (NO_3), and silicate (Si(OH)_4) (data were

339 previously published in Cao et al. (2012), Dai et al. (2013), and Du et al. (2013)) rapidly decrease from
340 the subsurface to the very surface waters near zero, DBa concentrations in the upper 150 m are almost
341 constant (Fig. 7). Surface DBa is not as strongly depleted as major nutrients largely because living
342 phytoplankton does not actively uptake Ba during growth (Fisher et al., 1991; Sternberg et al., 2005).
343 Below 150 m, DBa and Si(OH)_4 display a positive linear relationship which is, however, not observed
344 between DBa and PO_4 or NO_3 (Fig. 7). While PO_4 and NO_3 are labile nutrients controlled by shallower
345 recycling through the decomposition of organic tissue, Si(OH)_4 behaves as a refractory nutrient
346 characterized by deeper regeneration via dissolution of planktonic hard parts (Chan et al., 1977; Lea and
347 Boyle, 1989). In this context, regeneration of Ba in the deep ocean occurs at sites similar to Si(OH)_4 and
348 the covariance between these two parameters below the (sub)surface waters is largely a consequence of
349 ocean circulation (Lea and Boyle, 1989; Horner et al., 2015; Cao et al., 2016, 2020; Hsieh and
350 Henderson, 2017).

351 To further test if biological utilization of DBa significantly affects Ba isotopic compositions in the
352 surface waters, we compare our pBa_{xs} and biogenic particulate matter with Chl-a, which is
353 representative of total phytoplankton biomass (Fig. 8). Clearly, pBa_{xs} varies independently of Chl-a on
354 the NSCS outer shelf and slope and pBa_{xs} concentration ranges are similar at the lowest and highest Chl-
355 a conditions (Fig. 8a). In contrast, significant positive correlations are observed between pCa ($r^2=0.73$,
356 $n=23$), POC ($r^2=0.76$, $n=33$), PON ($r^2=0.90$, $n=33$), and BSi ($r^2=0.43$, $n=32$) and Chl-a and the highest
357 Chl-a concentrations are generally reflected by highest pCa, POC, PON, and BSi levels (Fig. 8b). We
358 suggest that pBa_{xs} formation is not directly associated with phytoplankton growth, making active
359 intracellular uptake of DBa from ambient seawater unlikely.

360 Another possible process inducing Ba isotope fractionation during DBa removal is barite formation.
361 Although a number of studies reached the conclusion that discrete barite crystals mainly precipitate in

the mesopelagic zone (e.g., Jacquet et al., 2008; Planchon et al., 2013; Lemaitre et al., 2018), barite has occasionally been observed in the upper water column as well (e.g., Bishop, 1988; Sternberg et al., 2008). This implies that our suspended particle samples in the upper 150 m of the NSCS might also contain barite. Therefore, the decoupling of Ba from carbon and major nutrients in both the dissolved and particulate phases suggests that passive adsorption onto particles instead of biological utilization of DBa most likely drives the Ba isotope fractionation in the upper NSCS, while the potential effect of barite formation needs further dedicated examination.

There are various potential Ba carriers for adsorption in the ocean including plankton (i.e, PIC, POC, PON, and BSi), iron-manganese (Fe-Mn) oxides, and lithogenic minerals (Dehairs et al., 1980; Bishop, 1988; Sternberg et al., 2005). However, the constant $\delta^{138}\text{Ba}_{\text{DBa}}$ and $\delta^{138}\text{Ba}_{\text{pBa bulk}}$ observed in the upper 150 m of the NSCS point to a single dominant carrier controlling Ba isotope fractionation. The decoupling of Ba from direct biological productivity indicators implies that plankton itself is not the main carrier. Our pAl data in the upper 150 m demonstrate that lithogenic components are negligible on the NSCS slope. Given that cross-shelf transport of particles enriched in Fe and Mn is highly likely, we suggest that Fe-Mn oxides are a potentially important Ba carrier in the upper water column on the NSCS outer shelf and slope. Sternberg et al. (2005) attributed the particulate Ba produced in laboratory diatom cultures to the adsorption onto precipitated Fe hydroxides associated with the cell surface rather than to the intracellular uptake. Nevertheless, future work is required to identify the specific carriers of Ba in the upper NSCS via analyzing different chemical leachates, examinations by scanning electron microscopy, and/or utilizing micro-analytical techniques.

4.2.3. Homogenous $\delta^{138}\text{Ba}_{\text{pBa xs}}$ signatures despite variable pBa_{xs} concentrations in the upper 150 m

In contrast to highly variable pBa_{xs} concentrations, the isotopic compositions of bulk and excess particulate Ba are remarkably homogenous. We were able to show that they are not produced directly by

385 biological productivity in the upper NSCS. Our study area is, overall, oligotrophic, and comparable
386 surface water productivities between stations are anticipated based on similar nutrient concentrations.
387 The variable pBa_{xs} concentrations in our suspended particle samples in the upper 150 m are likely
388 influenced by particle sinking and/or zooplankton grazing. Such processes would overall lower the
389 standing stock of excess particulate Ba relative to the corresponding total amount transformed from the
390 dissolved phase, but unlikely introduce additional isotope fractionation effects. In this context, the
391 $\delta^{138}Ba_{pBa_{xs}}$ signatures could integrate reliable information during transformation of DBa to pBa_{xs} ,
392 making the resulting signal independent of variations in pBa_{xs} concentrations that are also affected by
393 other processes. This implies that particulate Ba isotopes are likely a more robust proxy for total particle
394 fluxes than discrete bottle pBa_{xs} concentrations because the latter would rather reflect “snapshots” of the
395 water column at a particular time. However, whether the mechanisms inferred from Ba isotope data
396 from the NSCS can be adopted for other oceanic environments requires additional field work.

397 **4.3. Ba isotope fractionation factor in the upper NSCS**

398 *4.3.1. Estimations based on a Rayleigh and a steady state model*

399 The T-S distribution above 150 m depth (or the salinity maximum) shows comparable linear
400 relationships between stations (Fig. 2), which suggests that the upper water column on the NSCS outer
401 shelf and slope can be approximated as a uniform water mass. Using the average of DBa and $\delta^{138}Ba_{DBa}$
402 values collected from 300 m depth at stations A1, A10, and S504 as initial values and field $\delta^{138}Ba_{DBa}$
403 data collected in the upper 150 m at all sampling stations, the estimated in situ fractionation factor ($^{138}\epsilon$)
404 between particulate and dissolved Ba through point-by-point calculations averages $-0.4 \pm 0.1\text{‰}$ (1SD,
405 $n=27$) following a Rayleigh model (Supplementary Eq. (5)) and $-0.5 \pm 0.1\text{‰}$ (1SD, $n=27$) following a
406 steady state model (Supplementary Eq. (8)). Both values are within error identical to the apparent
407 fractionation factor $\Delta^{138}Ba$ (Supplementary Eq. (9)) of $-0.5 \pm 0.1\text{‰}$ (1SD, $n=19$) suggesting that the

408 estimated $^{138}\epsilon$ is realistic. This also demonstrates that our selection of an initial condition from
409 underlying deep waters at 300 m is valid, while the influence from horizontal mixing of the KBW could
410 be neglected. Note that any fractionation factors estimated based on field measurements reflect a
411 combined effect exerted by both physical and biogeochemical processes, whereas in this scenario the
412 mixing influence, though existent, would be small due to the isotope fractionation models were mainly
413 applied to data from effectively a single water mass. Details of the model estimation are provided in the
414 Supplementary Material and Supplementary Table 1.

415 4.3.2. *Comparison with previously reported values*

416 $^{138}\epsilon$ and $\Delta^{138}\text{Ba}$ values of -0.4 to -0.5‰ observed in the NSCS are within the range of -0.3 to -0.6‰
417 previously reported by field measurements (Horner et al., 2015, 2017; Cao et al., 2020; Bates et al., 2017;
418 Hsieh and Henderson, 2017; Bridgestock et al., 2018), despite that the specific depth range over which
419 DBa removal occurs is different between these studies. Our $\Delta^{138}\text{Ba}$ value is essentially identical to that
420 of $-0.53\pm0.04\text{‰}$ and $-0.41\pm0.09\text{‰}$, respectively, observed in the upper 200 m of the South Atlantic and
421 Lake Superior by Horner et al. (2017), which are the same as the difference between $\delta^{138}\text{Ba}_{\text{pBa bulk}}$ (or
422 $\delta^{138}\text{Ba}_{\text{pBa xs}}$) in suspended particles and $\delta^{138}\text{Ba}_{\text{DBa}}$ in waters. Such consistent values point to a constant Ba
423 isotope fractionation factor between bulk particles and seawater throughout the ocean (Bridgestock et al.,
424 2018).

425 $^{138}\epsilon$ and $\Delta^{138}\text{Ba}$ obtained in this study suggest a slightly larger in situ Ba isotope fractionation with the
426 same direction than those of -0.1 to -0.4‰ observed in inorganic precipitation experiments and/or
427 during coral growth (Böttcher et al., 2018, and references therein; Hemsing et al., 2018; Geyman et al.,
428 2019; Liu et al., 2019; Mavromatis et al., 2019). However, the mechanisms controlling Ba isotope
429 fractionation during incorporation into coral aragonite or high-Mg calcite are still unclear, in particular
430 in natural systems (Pretet et al., 2016; Hemsing et al., 2018; Geyman et al., 2019; Liu et al., 2019).

431 Mavromatis et al. (2019) even reported preferential incorporation of heavier Ba isotopes in inorganic
432 aragonite at very slow growth rates. The slightly larger fractionation observed in the upper NSCS may
433 be related to the in situ biologically-mediated transformation from DBa to pBa_{xs} such as adsorption onto
434 biogenic particles, which, however, needs to be further constrained by additional estimations of $^{138}\epsilon$ in
435 both real oceanic environments and laboratory culture experiments.

436 Adsorption-induced enrichment of lighter Ba isotopes in the particulate phase has also been observed
437 in soil (Gong et al., 2019) and river systems (Gou et al., 2020). However, a batch equilibrium
438 experiment for adsorption onto the surface of silica hydrogel revealed an opposite direction of Ba
439 isotope fractionation with heavier Ba isotopes being preferentially adsorbed ($\Delta^{138}\text{Ba}_{\text{gel-solution}} \sim +0.1$ to
440 $+0.3\text{‰}$; van Zuilen et al., 2016a). This contrast might result from the difference in mineral structure
441 between soils and hydrogel (Gong et al., 2019). Similar to other trace metals such as copper (e.g., Vance
442 et al., 2008) and molybdenum (e.g., Goldberg et al., 2009), Ba adsorption is most likely induced by its
443 strong interaction with nonmetallic elements or organometallic compounds. Nevertheless, the specific
444 mechanisms by which Ba is adsorbed onto marine particles and is isotopically fractionated are currently
445 unknown. The reason why the adsorption induces comparable removal of DBa and resulting identical
446 fractionation with constant $\delta^{138}\text{Ba}_{\text{DBa}}$ and $\delta^{138}\text{Ba}_{\text{pBa}_{\text{xs}}}$ in the upper NSCS needs further exploration.

447 5. CONCLUSIONS

448 The dynamics of $\delta^{138}\text{Ba}$ on the NSCS outer shelf and slope are primarily controlled by the
449 combination of vertical mixing from depth and fractionation in the upper water column. Preferential
450 adsorption of the lighter isotopes onto one major particulate phase most likely results in the homogenous
451 distribution of $\delta^{138}\text{Ba}_{\text{pBa}_{\text{xs}}}$ and $\delta^{138}\text{Ba}_{\text{DBa}}$ in the upper 150 m of the entire study area, with the former
452 systematically lighter than the latter by $\sim 0.5\text{‰}$. This value is essentially identical to the estimated $^{138}\epsilon$
453 following both the Rayleigh and steady state models suggesting a valid Ba isotope fractionation factor

454 between particulate and dissolved Ba in a natural system. This is consistent with previously reported
455 $\Delta^{138}\text{Ba}$ from other marine and freshwater settings. However, the specific carriers of Ba in the upper
456 NSCS still need to be identified and the fractionation via particle adsorption needs examination in other
457 oceanic environments.

458 The decoupling of DBa from NO_3 and PO_4 throughout the water column and from Si(OH)_4 in the
459 upper NSCS implies that although considered a nutrient-like element, Ba does not directly trace nutrient
460 utilization and regeneration. Stable Ba isotopes that correspond to DBa variations may thus not be a
461 proxy for nutrient cycling in the ocean. In addition, the constant $\delta^{138}\text{Ba}_{\text{pBa}_{\text{xs}}}$ signatures do not show a
462 clear link with surface biological productivity, which is supported by the lack of covariance between
463 pBa_{xs} and biogenic particulate matter in the upper NSCS. In order to clarify whether Ba isotopes may
464 nevertheless be a reliable proxy for paleoproductivity, comprehensive information on the isotopic
465 compositions of various Ba carriers, in particular barite, is needed from the very surface to the
466 mesopelagic zone to the sediments in oceanic environments with contrasting productivity levels.

467 **Acknowledgements**

468 This work was funded by the National Natural Science Foundation of China (91858107 and
469 41606089), the National Key Scientific Research Project (2015CB954003) sponsored by the Ministry of
470 Science and Technology of China, and the Fundamental Research Funds for the Central Universities
471 (20720180123). We would like to thank Yaojin Chen, Baomin Liu, Tao Huang, Lifang Wang, Danna
472 Wang, and Yanping Xu for help with the ancillary data collection and the crew of R/V *Dongfanghong II*
473 for their assistance in sample collection. We thank Yihua Cai for providing the GEOTRACES SAFe
474 seawater reference material, Jianyu Hu for providing the CTD data, Pinghe Cai for providing the POC
475 and PON data, and Jun Sun for providing the Chl-a data. John Hodgkiss is thanked for his assistance in
476 polishing the manuscript's English. Constructive comments by Susan Little, Gregory de Souza, and
477 three anonymous reviewers significantly improved the quality of this contribution.

478 **References**

- 479 Bacon M. P. and Edmond J. M. (1972) Barium at GEOSECS III in the Southwest Pacific. *Earth Planet.*
480 *Sci. Lett.* **16**, 66-74.
- 481 Bates S. L., Hendry K. R., Pryer H. V., Kinsley C. W., Pyle K. M., Woodward E. M. S. and Horner T. J.
482 (2017) Barium isotopes reveal role of ocean circulation on barium cycling in the Atlantic. *Geochim.*
483 *Cosmochim. Acta* **204**, 286-299.
- 484 Bernstein R. E. and Byrne R. H. (2004) Acantharians and marine barite. *Mar. Chem.* **68**, 45-50.
- 485 Bishop J. K. B. (1988) The barite-opal-organic carbon association in oceanic particulate matter. *Nature*
486 **332**, 341-343.
- 487 Bishop J. K. B. and Wood T. J. (2008) Particulate matter chemistry and dynamics in the twilight zone at
488 VERTIGO ALOHA and K2 sites. *Deep-Sea Res. I* **55**, 1684-1706.
- 489 Böttcher M. E., Neubert N., von Allmen K., Samankassou E. and Nögler T. F. (2018) Barium isotope
490 fractionation during the experimental transformation of aragonite to witherite and of gypsum to barite,
491 and the effect of ion (de)solvation. *Isot. Environ. Health Stud.* **54**, 324-335.
- 492 Bridgestock L., Hsieh Y.-T., Porcelli D., Homoky W. B., Bryan A. and Henderson G. M. (2018)
493 Controls on the barium isotope compositions of marine sediments. *Earth Planet. Sci. Lett.* **481**, 101-
494 110.
- 495 Bridgestock L., Hsieh Y.-T., Porcelli D., and Henderson G. M. (2019) Increased export production
496 during recovery from the Paleocene-Eocene thermal maximum constrained by sedimentary Ba
497 isotopes. *Earth Planet. Sci. Lett.* **510**, 53-63.
- 498 Cai P., Zhao D., Wang L., Huang B. and Dai M. (2015) Role of particle stock and phytoplankton
499 community structure in regulating particulate organic carbon export in a large marginal sea. *J.*
500 *Geophys. Res. Oceans* **120**, 2063-2095, doi:10.1002/2014JC010432.

501 Cao Z. and Dai M. (2011) Shallow-depth CaCO_3 dissolution: Evidence from excess calcium in the
 502 South China Sea and its export to the Pacific Ocean. *Global Biogeochem. Cycles* **25**, GB2019,
 503 doi:10.1029/2009GB003690.

504 Cao Z., Dai M., Lu Z. and Zhou K. (2009) CaCO_3 to organic carbon ratio in the South China Sea, in
 505 *Advances in Geosciences: Ocean Science*, edited by J. Gan et al., vol. 12, pp. 109-125, World
 506 Scientific Publishing Company.

507 Cao Z., Dai M., Zheng N., Wang D., Li Q., Zhai W., Meng F. and Gan J. (2011) Dynamics of the
 508 carbonate system in a large continental shelf system under the influence of both a river plume and
 509 coastal upwelling. *J. Geophys. Res.* **116**, G02010, doi:10.1029/2010JG001596.

510 Cao Z., Frank M., Dai M., Grasse P. and Ehlert C. (2012) Silicon isotope constraints on sources and
 511 utilization of silicic acid in the northern South China Sea. *Geochim. Cosmochim. Acta* **97**, 88-104.

512 Cao Z., Siebert C., Hathorne E. C., Dai M. and Frank M. (2016) Constraining the oceanic barium cycle
 513 with stable barium isotopes. *Earth Planet. Sci. Lett.* **434**, 1-9.

514 Cao Z., Siebert C., Hathorne E. C., Dai M. and Frank M. (2020) Corrigendum to “Constraining the
 515 oceanic barium cycle with stable barium isotopes” [Earth Planet. Sci. Lett. 434 (2016) 1-9]. *Earth*
 516 *Planet. Sci. Lett.* **530**, 116003.

517 Cardinal D., Dehairs F., Cattaldo T. and André L. (2001) Geochemistry of suspended particles in the
 518 Subantarctic and Polar Front Zones south of Australia: Constraints of export and advection processes.
 519 *J. Geophys. Res.* **106**, 31637-31656.

520 Chan L.-H., Drummond D., Edmond J. M. and Grant B. (1977) On the barium data from the Atlantic
 521 GEOSECS expedition. *Deep-Sea Res.* **24**, 613-649.

522 Carter S. C., Paytan A. and Griffith E. M. (2020) Toward an improved understanding of the marine
 523 barium cycle and the application of marine barite as a paleoproductivity proxy. *Minerals* **10**, 421.

524 Chao S. Y., Shaw P. T. and Wu S. Y. (1996) Deep water ventilation in the South China Sea. *Deep-Sea*
525 *Res. I* **43**, 445-466.

526 Chen Y.-L. L. (2005) Spatial and seasonal variations of nitrate-based new production and primary
527 production in the South China Sea. *Deep-Sea Res. I* **52**, 319-340.

528 Chen M., Liu H., Song S. and Sun J. (2015) Size-fractionated mesozooplankton biomass and grazing
529 impact on phytoplankton in northern South China Sea during four seasons. *Deep-Sea Res. II* **117**, 108-
530 118.

531 Crockford P. W., Wing B. A., Paytan A., et al. (2019) Barium-isotopic constraints on the origin of post-
532 Marinoan barites. *Earth Planet. Sci. Lett.* **519**, 234-244.

533 Dai M., Cao Z., Guo X., Zhai W., Liu Z., Yin Z., Xu Y., Gan J., Hu J. and Du C. (2013) Why are some
534 marginal seas sources of atmospheric CO₂?. *Geophys. Res. Lett.* **40**, 2154-2158,
535 doi:10.1002/grl.50390.

536 Dehairs F., Chesselet R. And Jedwab J. (1980) Discrete suspended particles of barite and the barium
537 cycle in the open Ocean. *Earth Planet. Sci. Lett.* **49**, 528-550.

538 Dehairs F., Jacquet S., Savoye N., Van Mooy B. A. S., Buesseler K. O., Bishop J. K. B., Lamborg C. H.,
539 Elskens M., Baeyens W., Boyd P. W., Casciotti K. L. and Monnin C. (2008) Barium in twilight zone
540 suspended matter as a potential proxy for particulate organic carbon remineralization: Results for the
541 North Pacific. *Deep-Sea Res. II* **55**, 1673-1683.

542 Dehairs F., Shopova D., Ober S., Veth C. and Goeyens L. (1997) Particulate barium stocks and oxygen
543 consumption in the Southern Ocean mesopelagic water column during spring and early summer:
544 relationship with export production. *Deep-Sea Res. II* **44**, 497-516.

545 Du C., Liu Z., Dai M., Kao S.-J., Cao Z., Zhang Y., Huang T., Wang L. and Li Y. (2013) Impact of the
 546 Kuroshio intrusion on the nutrient inventory in the upper northern South China Sea: insights from an
 547 isopycnal mixing model. *Biogeosciences* **10**, 6419-6432.

548 Esser B. K. and Volpe A. M. (2002) At-sea high-resolution chemical mapping: extreme barium
 549 depletion in North Pacific surface water. *Mar. Chem.* **79**, 67-79.

550 Fisher N. S., Guillard R. R. L. and Bankston D. C. (1991) The accumulation of barium by marine
 551 phytoplankton grown in culture. *J. Mar. Res.* **49**, 339-354.

552 François R., Honjo S., Manganini S. J. and Ravizza G. E. (1995) Biogenic barium fluxes to the deep sea:
 553 Implications for paleoproductivity reconstructions. *Global Biogeochem. Cycles* **9**, 289-303.

554 Freydier R., Dupre B. and Polve M. (1995) Analyses by inductively coupled plasma mass spectrometry
 555 of Ba concentrations in water and rock samples. Comparison between isotope dilution and external
 556 calibration with or without internal standard. *Eur. Mass Spectrom.* **1**, 283-291.

557 Gan J., Liu Z. and Hui C. (2016) A three-layer alternating spinning circulation in the South China Sea. *J.*
 558 *Phys. Oceanogr.* **46**, 2309-2315.

559 Ganeshram R. S., François R., Commeau J. and Brown-Leger S. L. (2003) An experimental
 560 investigation of barite formation in seawater. *Geochim. Cosmochim. Acta* **67**, 2599-2605.

561 Geyman B. M., Ptacek J. L., LaVigne M. and Horner T. J. (2019) Barium in deep-sea bamboo corals:
 562 Phase associations, barium stable isotopes, & prospects for paleoceanography. *Earth Planet. Sci. Lett.*
 563 **525**, 115751.

564 Goldberg T., Archer C., Vance D. and Poulton S. W. (2009) Mo isotope fractionation during adsorption
 565 to Fe (oxyhydr)oxides. *Geochim. Cosmochim. Acta* **73**, 6502-6516.

566 Gong Y., Zeng Z., Zhou C., Nan X., Yu H., Lu Y., Li W., Gou W., Cheng W. and Huang F. (2019)
567 Barium isotopic fractionation in latosol developed from strongly weathered basalt. *Sci. Total Environ.*
568 **687**, 1295-1304.

569 González-Muñoz M. T., Luque B. F., Ruiz F. M., Chekroun K. B., Arias J. M., Gallego M.R., Canamero
570 M. M., deLinares C. and Paytan A. (2003) Precipitation of barite by *Myxococcus xanthus*: Possible
571 implications for the biogeochemical cycle of barium. *Appl. Environ. Microbiol.* **69**,
572 doi:10.1128/AEM.69.9.5722-5725, 5722-5725.

573 Gou L.-F., Jin Z., Galy A., Gong Y.-Z., Nan X.-Y., Jin C., Wang X.-D., Bouchez J., Cai H.-M., Chen J.-
574 B., Yu H.-M. and Huang F. (2020) Seasonal riverine barium isotopic variation in the middle Yellow
575 River: Sources and fractionation. *Earth Planet. Sci. Lett.* **531**, 115990.

576 Grosse J., Bombar D., Doan H. N., Nguyen L. N. and Voss M. (2010) The Mekong River plume fuels
577 nitrogen fixation and determines phytoplankton species distribution in the South China Sea during
578 low and high discharge season. *Limnol. Oceanogr.* **55**, 1668-1680.

579 Guay C. K. and Falkner K. K. (1998) A survey of dissolved barium in the estuaries of major Arctic
580 rivers and adjacent seas. *Cont. Shelf Res.* **18**, 859-882.

581 Hall J. M. and Chan L.-H. (2004) Ba/Ca in benthic foraminifera: Thermocline and middepth circulation
582 in the North Atlantic during the last glaciation. *Paleoceanography* **19**, PA4018,
583 doi:10.1029/2004PA001028.

584 Hemsing F., Hsieh Y.-T., Bridgestock L., Spooner P. T., Robinson L. F., Frank, N., and Henderson G.M.
585 (2018) Barium isotopes in cold-water corals. *Earth Planet. Sci. Lett.* **491**, 183-192.

586 Horner T. J., Kinsley, C. W. and Nielsen S. G. (2015) Barium-isotopic fractionation in seawater
587 mediated by barite cycling and ocean circulation. *Earth Planet. Sci. Lett.* **430**, 511-522.

588 Horner T. J., Pryer H. V., Nielsen S. G., Crockford P. W., Gauglitz J. M., Wing B. A. and Ricketts R. D.
 589 (2017) Pelagic barite precipitation at micromolar ambient sulfate. *Nat. Commun.* **8**, 1242.
 590 Hsieh Y.-T. and Henderson G. M. (2017) Barium stable isotopes in the global ocean: Tracer of Ba
 591 inputs and utilization. *Earth Planet. Sci. Lett.* **473**, 269-278.
 592 Jacquet S. H. M., Dehairs F., Dumont I., Becquevort S., Cavagna A.-J. and Cardinal D. (2011) Twilight
 593 zone organic carbon remineralization in the Polar Front Zone and Subantarctic Zone south of
 594 Tasmania. *Deep-Sea Res. II* **58**, 2222-2234.
 595 Jacquet S. H. M., Dehairs F., Elskens M., Savoye N. and Cardinal D. (2007) Barium cycling along
 596 WOCE SR3 line in the Southern Ocean. *Mar. Chem.* **106**, 33-45.
 597 Jacquet S. H. M., Dehairs F., Lefèvre D., Cavagna A. J., Planchon F., Christaki U., Monin, L., André L.,
 598 Closset I. and Cardinal D. (2015) Early spring mesopelagic carbon remineralization and transfer
 599 efficiency in the naturally iron-fertilized Kerguelen area. *Biogeosciences* **12**, 1713-1731.
 600 Jacquet S. H. M., Monnin C., Riou V., Jullion L. and Tanhua T. (2016) A high resolution and quasi-
 601 zonal transect of dissolved Ba in the Mediterranean Sea. *Mar. Chem.* **178**, 1-7.
 602 Jacquet S. H. M., Dehairs F., Savoye N., Obernosterer I., Christaki U., Monnin C. and Cardinal D. (2008)
 603 Mesopelagic organic carbon mineralization in the Kerguelen Plateau region tracked by biogenic
 604 particulate Ba. *Deep-Sea Res. II* **55**, 868-879.
 605 Jeandel C., Tachikawa K., Bory A. and Dehairs F. (2000) Biogenic barium in suspended and trapped
 606 material as a tracer of export production in the tropical NE Atlantic (EUMELI sites). *Mar. Chem.* **71**,
 607 125-142.
 608 Klinkhammer G. P. and Chan L. H. (1990) Determination of barium in marine waters by isotope dilution
 609 inductively coupled plasma mass spectrometry. *Anal. Chim. Acta* **232**, 323- 329.

610 Lea D. and Boyle E. (1989) Barium content of benthic foraminifera controlled by bottom-water
611 composition. *Nature* **338**, 751-753.

612 Lemaitre N., Planquette H., Planchon, F., et al. (2018) Particulate barium tracing of significant
613 mesopelagic carbon remineralisation in the North Atlantic. *Biogeosciences* **15**, 2289-2307.

614 Liu K.-K., Chao S.-Y., Shaw P.-T., Gong G.-C., Chen C.-C. and Tang T. Y. (2002) Monsoon-forced
615 chlorophyll distribution and primary production in the South China Sea: observations and a numerical
616 study. *Deep-Sea Res. I* **49**, 1387-1412.

617 Liu Y., Li X., Zeng Z., Yu H.-M., Huang F., Felis T. and Shen C.-C. (2019) Annually-resolved coral
618 skeletal d138/134Ba records: A new proxy for oceanic Ba cycling. *Geochim. Cosmochim. Acta* **247**,
619 27-39.

620 Martinez-Ruiz F., Jroundi F., Paytan A., Guerra-Tschuschke I., Abad M. D. and Gonzalez-Munoz M. T.
621 (2018) Barium bioaccumulation by bacterial biofilms and implications for Ba cycling and use of Ba
622 proxies. *Nat. Commun.* **9**, DOI:10.1038/s41467-018-04069-z.

623 Mavromatis V., van Zuilen K., Blanchard M., van Zuilen M., Dietzel M. and Schott J. (2019)
624 Experimental and theoretical modelling of kinetic and equilibrium Ba isotope fractionation during
625 calcite and aragonite precipitation. *Geochim. Cosmochim. Acta*, doi:
626 <https://doi.org/10.1016/j.gca.2019.11.007>.

627 Mavromatis V., van Zuilen K., Purgstaller B., Baldermann A., Nägler T. F. and Dietzel M. (2016)
628 Barium isotope fractionation during witherite (BaCO₃) dissolution, precipitation and at equilibrium.
629 *Geochim. Cosmochim. Acta* **190**, 72-84.

630 McManus J., Berelson W. M., Klinkhammer G. P., Johnson K. S., Coale K. H., Anderson R. F., Kumar
631 N., Burdige D. J., Hammond D. E., Brumsack H. J., McCorkle D. C. and Rushdi A. (1998)

632 Geochemistry of barium in marine sediments: Implications for its use as a paleoproxy. *Geochimi.*
633 *Cosmochim. Acta* **62**, 3453-3473.

634 Monnin C., Jeandel C., Cattaldo T. and Dehairs F. (1999) The marine barite saturation state of the
635 world's oceans. *Mar. Chem.* **65**, 253-261.

636 Nan X., Yu H.-M., Rudnick R. L., Gasching R. M., Xu J., Li W.-Y., Zhang Q., Jin Z.-D., Li X.-H. and
637 Huang F. (2018) Barium isotopic composition of the upper continental crust. *Geochim. Cosmochim.*
638 *Acta* **233**, 33-49.

639 Nielsen S. G., Horner T. J., Pryer H. V., Blusztajn J., Shu Y., Kurz M. D. and Le Roux V. (2018)
640 Barium isotope evidence for pervasive sediment recycling in the upper mantle. *Sci. Adv.* **4**, eaas8675.

641 Planchon F., Cavagna A.-J., Cardinal D., André L. and Deharis F. (2013) Late summer particulate
642 organic carbon export and twilight zone remineralisation in the Atlantic sector of the Southern Ocean.
643 *Biogeosciences* **10**, 803-820.

644 Pretet C., van Zuilen K., Nägler T. F., Reynaud S., Böttcher M. E. and Samankassou E. (2016)
645 Constraints on barium isotope fractionation during aragonite precipitation by corals. *Depositional Rec.*
646 **1**, 118-129.

647 Redfield A. C., Ketchum B. H. and Richards F. A. (1963) The influence of organisms on the
648 composition of seawater, in *The Sea*, edited by Hill M. N., pp. 26-77, Wiley, New York.

649 Schlitzer R. (2019) Ocean Data View 5. <http://odv.awi.de>.

650 Siebert C., Nägler T. F. and Kramers J. D. (2001) Determination of molybdenum isotope fractionation
651 by double-spike multicollector inductively coupled plasma mass spectrometry. *Geochem. Geophys.*
652 *Geosyst.* **2**, 1032, doi:10.1029/2000GC000124.

653 Sternberg E., Jeandel C., Robin E. and Souhaut M. (2008) Seasonal cycle of suspended barite in the
654 mediterranean sea. *Geochim. Cosmochim. Acta* **72**, 4020-4034.

655 Sternberg E., Tang D., Ho T.-Y., Jeandel C. and Morel, F. M. M. (2005). Barium uptake and adsorption
656 in diatoms. *Geochim. Cosmochim. Acta* **69**, 2745-2752.

657 Suga T., Kato A. and Hanawa K. (2000) North Pacific Tropical Water: its climatology and temporal
658 changes associated with the climate regime shift in the 1970s. *Prog. Oceanogr.* **47**, 223-256.

659 Taylor S. R. and McLennan S. M. (1985). The continental crust: its composition and evolution.
660 Blackwell Scientific Publications, Melbourne, Australia, 312pp.

661 Tian J., Yang Q. and Zhao W. (2009) Enhanced diapycnal mixing in the South China Sea. *J. Phys.*
662 *Oceanogr.* **39**, 3191-3203.

663 van Beek P., Sternberg E., Reyss J.-L., Souhaut M., Robin E. and Jeandel C. (2009) $^{228}\text{Ra}/^{226}\text{Ra}$ and
664 $^{226}\text{Ra}/\text{Ba}$ ratios in the Western Mediterranean Sea: Barite formation and transport in the water column.
665 *Geochim. Cosmochim. Acta* **73**, 4720-4737.

666 van Zuilen K., Müller T., Nägler T. F., Dietzel M. and Küsters T. (2016a) Experimental determination
667 of barium isotope fractionation during diffusion and adsorption processes at low temperatures.
668 *Geochim. Cosmochim. Acta* **186**, 226-241.

669 van Zuilen K., Nägler T. F. and Bullen, T. D. (2016b) Barium isotopic compositions of geological
670 reference materials. *Geostand. Geoanal. Res.*, doi:10.1111/ggr.12122.

671 Vance D., Archer C., Bermin J., Perkins J., Statham P. J., Lohan M. C., Ellwood M. J. and Mills R. A.
672 (2008) The copper isotope geochemistry of rivers and the oceans. *Earth Planet. Sci. Lett.* **274**, 204-
673 213.

674 Weldeab S., Lea D. W., Schneider R. R. and Andersen N. (2007) 155,000 years of West African
675 monsoon and ocean thermal evolution. *Science* **316**, 1303-1307.

676 Winckler G., Anderson R. F., Jaccard S. L. and Marcantonio F. (2016) Ocean dynamics, not dust, have
677 controlled equatorial Pacific productivity over the past 500,000 years. *P. Natl. Acad. Sci.* **113**, 6119-
678 6124.

679 Wong G. T. F., Ku T.-L., Mulholland M., Tseng C.-M. and Wang D.-P. (2007) The South East Asian
680 Time-series Study (SEATS) and the biogeochemistry of the South China Sea-An overview. *Deep-Sea*
681 *Res. II* **54**, 1434-1447.

682 Yu Y., Siebert C., Fietzke J., Goepfert T., Hathorne E., Cao Z. and Frank M. (2020) The impact of MC-
683 ICP-MS plasma conditions on the accuracy and precision of stable isotope measurements evaluated
684 for barium isotopes. *Chem. Geol.* **549**, 119697.

685 You Y. (2003) The pathway and circulation of North Pacific Intermediate Water. *Geophys. Res. Lett.* **30**,
686 2291, doi:10.1029/2003GL018561.

687 **Table 1**

688 Dissolved barium (DBa) concentration and their stable barium isotopic composition ($\delta^{137}\text{Ba}_{\text{DBa_NIST}}$ and
689 $\delta^{138}\text{Ba}_{\text{DBa_NIST}}$) data collected in the northern South China Sea in January 2010.

Station	Depth (m)	Salinity	DBa (nmol kg ⁻¹)	$\delta^{137}\text{Ba}_{\text{DBa_NIST}} \pm 2\text{SD}^{\text{a}}$ (‰)	$\delta^{138}\text{Ba}_{\text{DBa_NIST}} \pm 2\text{SD}^{\text{b}}$ (‰)	n ^c
A5 ^d	5.9	34.41	33.4	0.45±0.03	0.60±0.04	3
21.0°N	25.4	34.41	33.2	0.43±0.07	0.58±0.09	3
115.0°E			duplicate	0.39±0.06	0.52±0.08	3
	51.1	34.45	31.6			
	73.0	34.42	31.9	0.44±0.06	0.59±0.08	3
			duplicate	0.40±0.02	0.53±0.02	3
	96.0	34.41	33.8	0.44±0.05	0.58±0.07	3
A2 ^d	3.1	34.17	33.5	0.44±0.10	0.59±0.14	3
20.5°N	24.2	34.17	33.3	0.47±0.03	0.63±0.04	3
115.4°E			duplicate	0.46±0.01	0.61±0.02	3
	47.6	34.26	33.7			
	73.3	34.30	34.1	0.46±0.03	0.62±0.05	3
	99.2	34.57	33.7			
	122.9	34.66	34.5	0.41±0.04	0.55±0.05	3
			duplicate	0.42±0.09	0.56±0.12	3
	149.5	34.67	34.3	0.44±0.03	0.58±0.04	3
	198.4	34.58	37.3			
	298.4	34.46	51.2			
A1	5.6	34.07	34.5	0.43±0.06	0.57±0.07	2
20.1°N	25.0	34.07	34.7	0.46±0.03	0.62±0.04	3
115.7°E			duplicate	0.48±0.03	0.64±0.04	3
	51.9	34.07	33.1	0.43±0.07	0.57±0.09	3
			duplicate	0.49±0.06	0.65±0.09	3
	74.8	34.43	34.4	0.46±0.06	0.62±0.08	3
	99.0	34.52	32.9	0.45±0.05	0.60±0.06	2
	124.8	34.58	34.3			
	148.1	34.57	36.4	0.42±0.02	0.55±0.03	3
	197.9	34.51	40.4	0.41±0.05	0.55±0.06	3
	300.0	34.42	49.9	0.36±0.12	0.48±0.16	3
			duplicate	0.39±0.08	0.51±0.11	3
	497.5	34.42	71.9	0.26±0.01	0.35±0.02	3
			duplicate	0.28±0.06	0.38±0.08	3
A10 ^d	6.2	33.80	36.2	0.47±0.02	0.63±0.02	2
19.2°N			duplicate	0.48±0.06	0.63±0.08	3
116.5°E	25.2	33.80	36.0	0.46±0.07	0.61±0.10	3
	50.1	33.82	36.1			

	75.6	34.29	34.0	0.47±0.08	0.63±0.10	3
	99.1	34.41	35.4			
	125.0	34.49	34.5	0.44±0.03	0.59±0.03	3
	150.1	34.65	34.4	0.45±0.02	0.60±0.03	3
	198.6	34.55	36.6	0.41±0.02	0.54±0.03	3
	300.2	34.44	56.2	0.31±0.03	0.42±0.04	3
			duplicate	0.35±0.08	0.47±0.10	3
	499.7	34.41	64.9			
	799.3	34.46	85.3	0.26±0.02	0.35±0.03	3
	998.9	34.51	99.6	0.23±0.03	0.31±0.03	3
S504	5.1	33.77	34.9	0.45±0.05	0.60±0.07	3
19.7°N			duplicate	0.48±0.01	0.64±0.01	3
117.6°E	25.1	33.77	34.8	0.44±0.01	0.59±0.02	3
	51.2	33.77	35.3	0.43±0.03	0.57±0.05	3
	75.8	33.77	34.8	0.47±0.05	0.63±0.07	3
	100.7	34.49	33.9	0.44±0.02	0.59±0.03	3
			duplicate	0.47±0.09	0.62±0.11	3
	123.8	34.56	34.8	0.42±0.01	0.56±0.01	3
	150.4	34.58	37.5	0.40±0.02	0.53±0.03	3
	200.8	34.55	37.7			
	299.7	34.46	47.8	0.31±0.02	0.42±0.03	3
	500.4	34.41	67.4			
	801.0	34.47	86.9	0.25±0.05	0.33±0.06	3
			duplicate	0.23±0.04	0.31±0.05	3
	1000.8	34.52	102.5	0.24±0.03	0.32±0.03	3
			duplicate	0.24±0.04	0.32±0.05	3

^a SD is the standard deviation estimated from the double spike bracketing measurements of a single sample solution.

^b $\delta^{138}\text{Ba}_{\text{DBa_NIST}} \pm 2\text{SD}$ is converted from $\delta^{137}\text{Ba}_{\text{DBa_NIST}} \pm 2\text{SD}$ by multiplying by 1.33 assuming mass-dependent fractionation.

^c n is the number of double spike bracketing measurements of a single sample solution.

^d Salinity data collected at stations A5, A2, and A10 were previously published in Cao et al. (2012).

696 **Table 2**

697 Bulk particulate barium (pBa_{bulk}) concentration and their stable barium isotopic composition
698 ($\delta^{137}\text{Ba}_{\text{pBa}_{\text{bulk_NIST}}}$ and $\delta^{138}\text{Ba}_{\text{pBa}_{\text{bulk_NIST}}}$) data collected in the upper 150 m of the northern South China
699 Sea in January 2010.

Station	Depth (m)	pBa _{bulk} (pmol kg ⁻¹)	$\delta^{137}\text{Ba}_{\text{pBa}_{\text{bulk_NIST}}}\pm 2\text{SD}^{\text{a}}$ (‰)	$\delta^{138}\text{Ba}_{\text{pBa}_{\text{bulk_NIST}}}\pm 2\text{SD}^{\text{b}}$ (‰)	n ^c
A5	25	351	0.14±0.04	0.19±0.05	3
21.0°N	75	234			
115.0°E					
A2	25	644	0.09	0.12	1
20.5°N	75	809	0.08±0.07	0.11±0.09	3
115.4°E	125	579	0.04±0.08	0.05±0.10	3
A1	5	374	0.16±0.15	0.21±0.21	3
20.1°N	25	297	0.16±0.04	0.21±0.05	3
115.7°E	50	411	0.11±0.08	0.15±0.10	3
	75	920	0.11±0.07	0.15±0.10	2
	100	508	0.07	0.10	1
	125	695	0.04±0.03	0.06±0.05	3
	150	926	0.03±0.06	0.04±0.07	2
A10	25	690	0.09±0.03	0.12±0.04	3
19.2°N	75	754	0.09±0.09	0.11±0.12	3
116.5°E	125	477			
	150	964	0.05	0.07	1
S504	5	363	0.13±0.05	0.17±0.07	3
19.7°N	25	305	0.16±0.02	0.21±0.03	3
117.6°E	50	380	0.16±0.09	0.21±0.11	2
	75	378	0.14±0.05	0.18±0.07	2
	100	649	0.07±0.01	0.09±0.01	3
	125	700			
	150	1056	0.04±0.05	0.06±0.06	3

700 ^a SD is the standard deviation estimated from the double spike bracketing measurements of a single
701 sample solution.

702 ^b $\delta^{138}\text{Ba}_{\text{pBa}_{\text{bulk_NIST}}}\pm 2\text{SD}$ is converted from $\delta^{137}\text{Ba}_{\text{pBa}_{\text{bulk_NIST}}}\pm 2\text{SD}$ by multiplying by 1.33 assuming
703 mass-dependent fractionation.

704 ^c n is the number of double spike bracketing measurements of a single sample solution.

705 **Table 3**

706 Concentration data of bulk and excess particulate barium (pBa_{bulk} and pBa_{xs}), particulate aluminum and calcium (pAl and pCa), particulate organic
 707 carbon and nitrogen (POC and PON), biogenic silica (BSi), and chlorophyll a (Chl-a) collected in the upper 150 m of the northern South China Sea in
 708 January 2010.

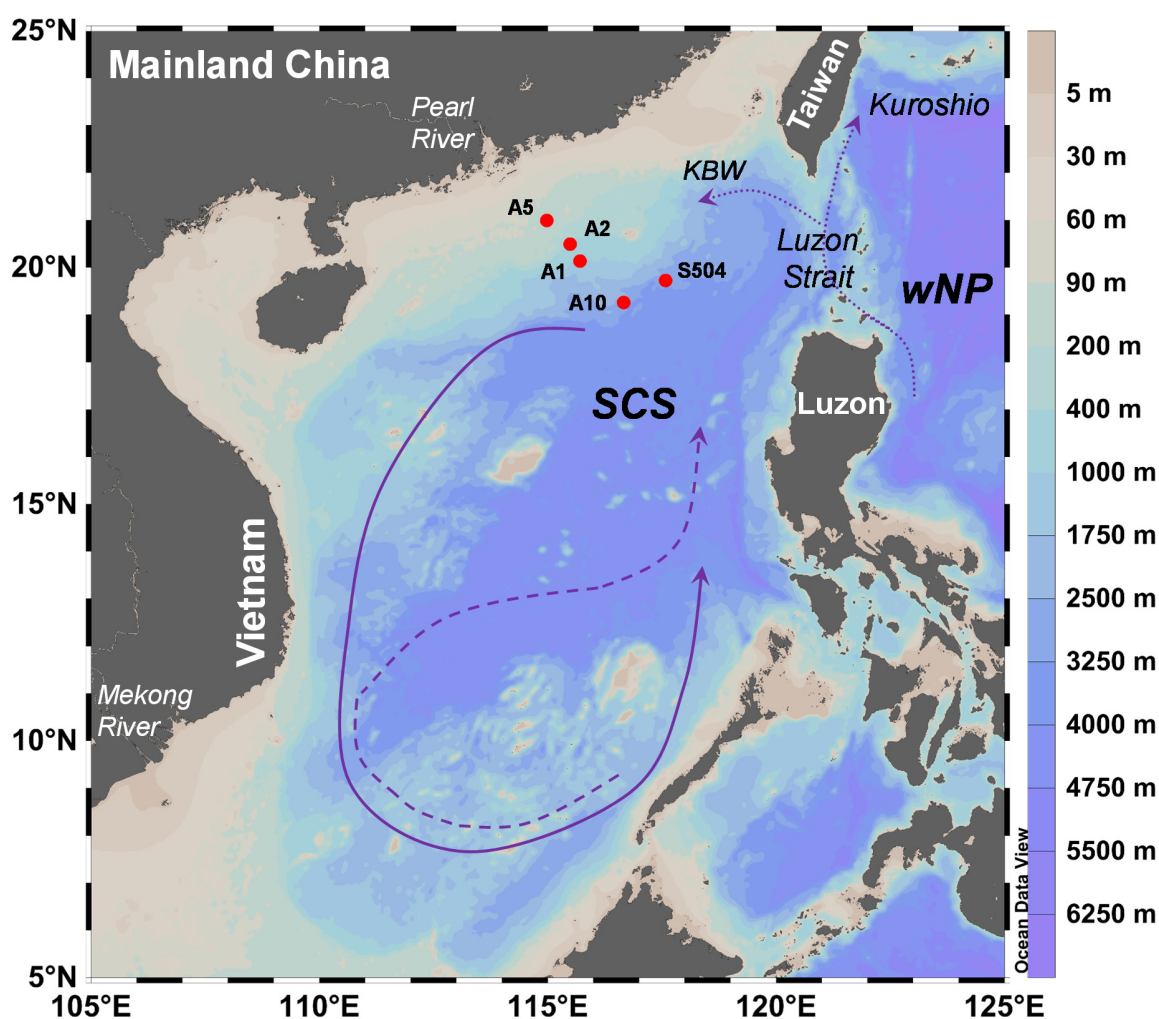
Station	Depth (m)	pBa_{bulk} ($pmol\ kg^{-1}$)	pBa_{xs} ($pmol\ kg^{-1}$)	pBa_{xs}/pBa_{bulk} (%)	pAl ($nmol\ kg^{-1}$)	pCa ($nmol\ kg^{-1}$)	POC ^a ($\mu mol\ L^{-1}$)	PON ^a ($\mu mol\ L^{-1}$)	BSi ($\mu mol\ L^{-1}$)	Chl-a ^b ($\mu g\ L^{-1}$)
A5	5						4.26	0.71	0.22	0.48
21.0°N	25	351	288	82	46.7	207.3	3.65	0.55	0.26	0.51
115.0°E	50						3.04	0.47	0.28	0.50
	75	235	171	73	47.3	262.7	3.33	0.58	0.26	0.43
	100						2.64	0.37	0.20	0.35
A2	5						3.02	0.49	0.23	0.50
20.5°N	25	648	630	97	13.4	225.0	3.78	0.54	0.26	0.46
115.4°E	50						3.43	0.56	0.48	0.61
	75	813	795	98	13.8	246.7	3.30	0.51	0.56	0.51
	100						1.18	0.17	0.19	0.07
	125	584	490	84	69.3	79.4	0.90	0.15	0.11	0.03
	150						0.88	0.12	0.10	0.03
A1	5	379	357	94	16.2	290.7	3.01	0.45	0.20	0.48
20.1°N	25	301	290	96	7.9	260.4	3.20	0.45	0.20	0.47
115.7°E	50	415	405	98	7.6	282.6	3.59	0.49	0.20	0.49
	75	924	891	96	24.5	163.1	3.06	0.31	0.18	0.20
	100	513	486	95	19.7	122.5	1.58	0.19	0.19	0.09
	125	700	658	94	30.8	114.5	1.81	0.15	0.13	0.04
	150	931	894	96	27.2	96.6	2.13	0.13	0.13	0.01
A10	5						2.86	0.48	0.16	0.53
19.2°N	25	694	675	97	14.5	153.9	3.28	0.58	0.17	0.54
116.5°E	50						2.97	0.48	0.17	0.53
	75	759	740	98	13.9	199.2	2.61	0.36	0.41	0.32
	100						0.86	0.16	0.14	0.05
	125	481	456	95	18.8	86.2	1.33	0.20	0.12	0.02

	150	968	914	94	40.5	79.3	0.69	0.12	0.09	0.02
S504	5	368	361	98	4.9	237.4	3.63	0.67	0.37	0.56
19.7°N	25	310	296	95	10.7	187.6	5.35	0.60	0.39	0.50
117.6°E	50	385	373	97	8.6	189.6	3.46	0.50	0.38	0.56
	75	382	372	97	7.5	136.3	2.21	0.35	0.18	0.35
	100	654	617	94	27.3	80.4	1.08	0.15	0.11	0.12
	125	704	690	98	10.7	96.8	1.03	0.12	0.08	0.06
	150	1061	1034	97	20.0	92.5	1.11	0.13		0.01

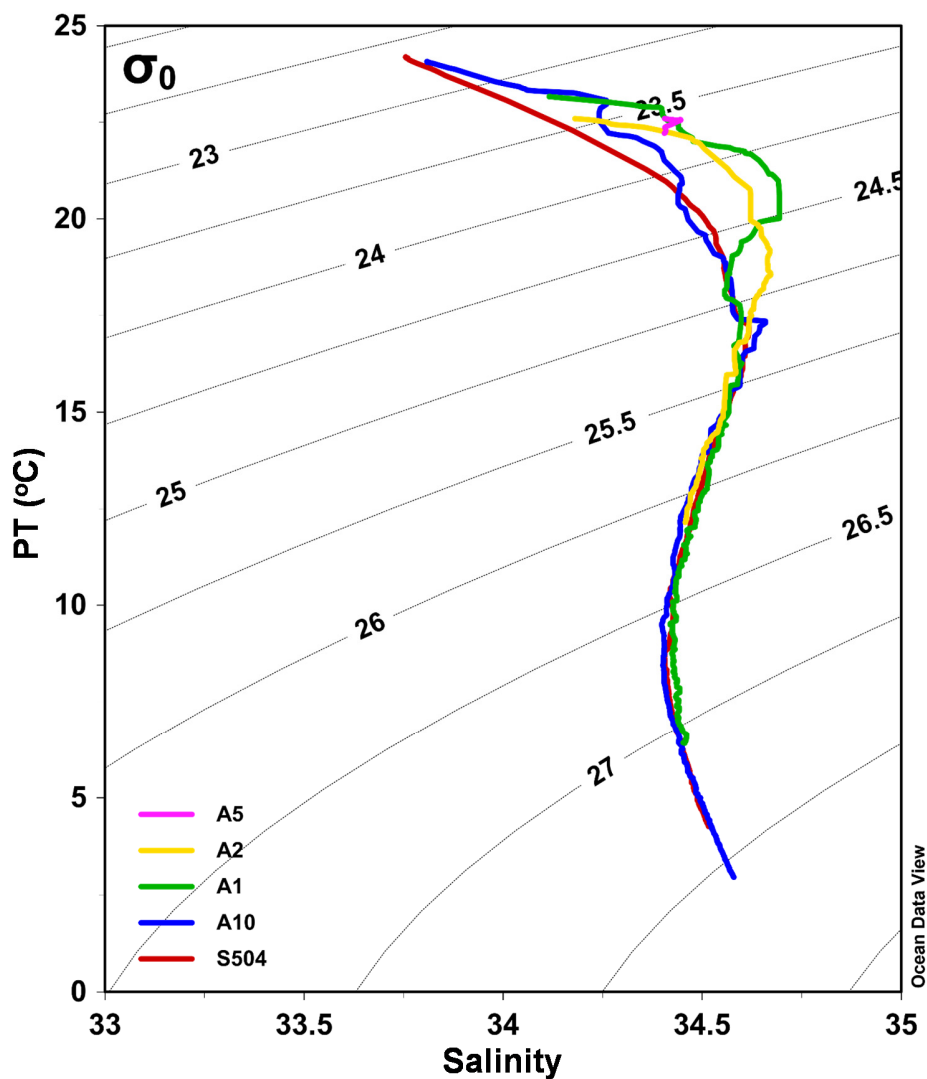
709 ^aPOC and PON data were previously published in Cai et al. (2015).

710 ^bChl-a data were previously published in Chen et al. (2015).

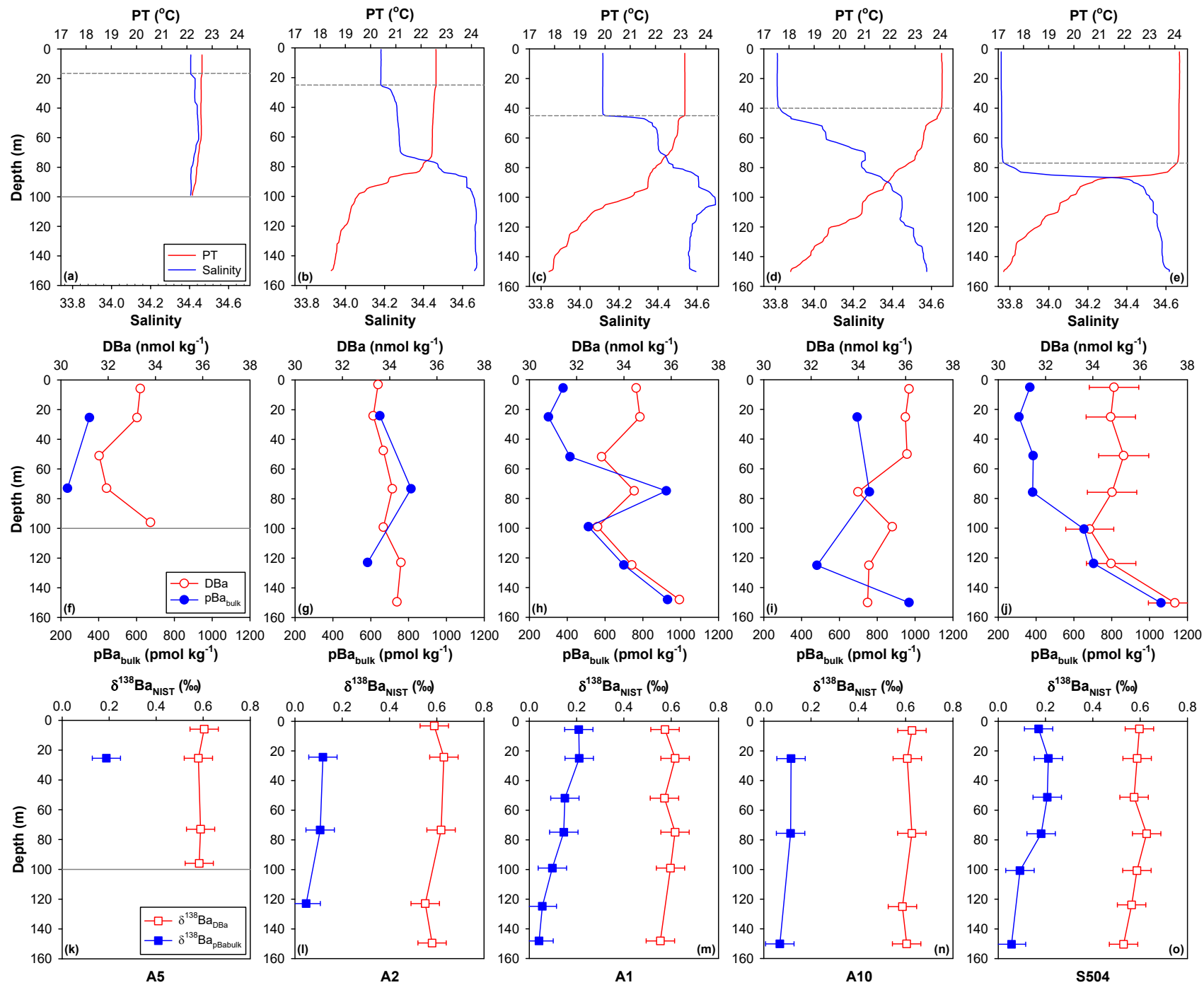
711 **Figure 1.** Bathymetric map of the South China Sea (SCS) showing the locations of sampling stations in January
 712 2010. The basin scale circulation pattern is according to Wong et al. (2007, and references therein), showing a
 713 basin wide cyclonic gyre in winter (solid line) and an anticyclonic gyre over the southern half of the SCS in
 714 summer (dashed line). Also shown schematically are the Kuroshio current and its intrusions into the northern
 715 SCS around the Luzon Strait (dotted line) according to Wong et al. (2007, and references therein). wNP:
 716 western North Pacific; KBW: Kuroshio Branch Water. The map was created with ODV (Schlitzer, 2019).



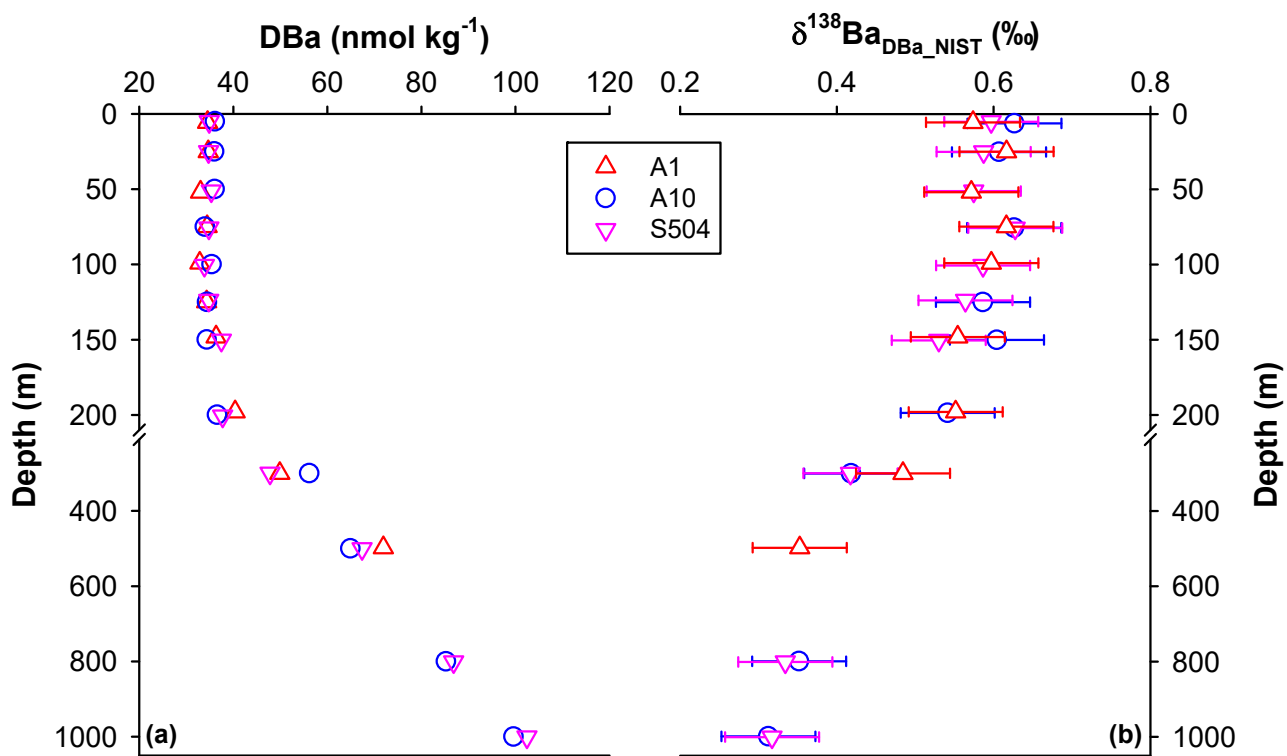
718 **Figure 2.** Potential temperature (PT) versus salinity plot (T-S diagram) for the sampling stations in the northern
719 South China Sea. The dashed lines indicate the isopycnals (σ_0). The plot was created with ODV (Schlitzer,
720 2019).



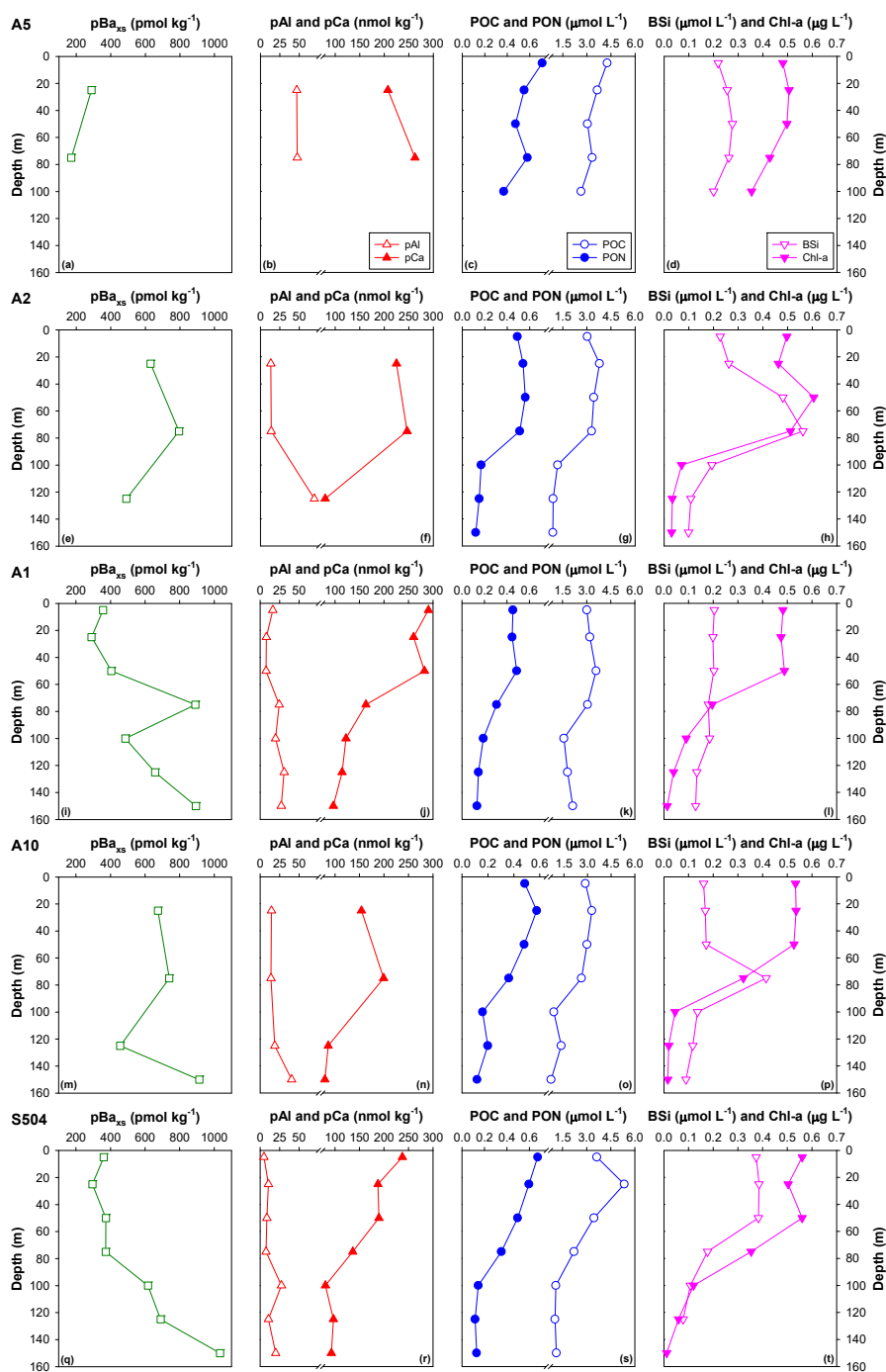
722 **Figure 3.** Vertical distributions of (a-e) potential temperature (PT) and salinity, (f-j) dissolved barium (DBa) and bulk particulate barium (pBa_{bulk})
723 concentrations, and (k-o) their stable barium isotopic compositions ($\delta^{138}\text{Ba}_{\text{DBa}}$ and $\delta^{138}\text{Ba}_{\text{pBa}_{\text{bulk}}}$) in the upper 150 m of the northern South China Sea.
724 The bottom depths of stations A5, A2, A1, A10, and S504 are ~100 m, ~400 m, ~850 m, ~2800 m and ~3100 m. The dashed horizontal line in (a)-(e)
725 denotes the depth of surface mixed layer. The solid horizontal line in (a), (f), and (k) denotes the bottom depth of station A5. In (j), error bars of DBa
726 representing $\pm 3\%$ (2 standard deviation, 2SD) of the field values are illustrated at station S504, which displays the largest difference in DBa
727 concentrations in the upper 150 m. Errors bars of $\delta^{138}\text{Ba}$ in (k)-(o) of this figure and those of all field $\delta^{138}\text{Ba}$ data in the following figures represent
728 the long-term external 2SD reproducibility of $\pm 0.06\%$.



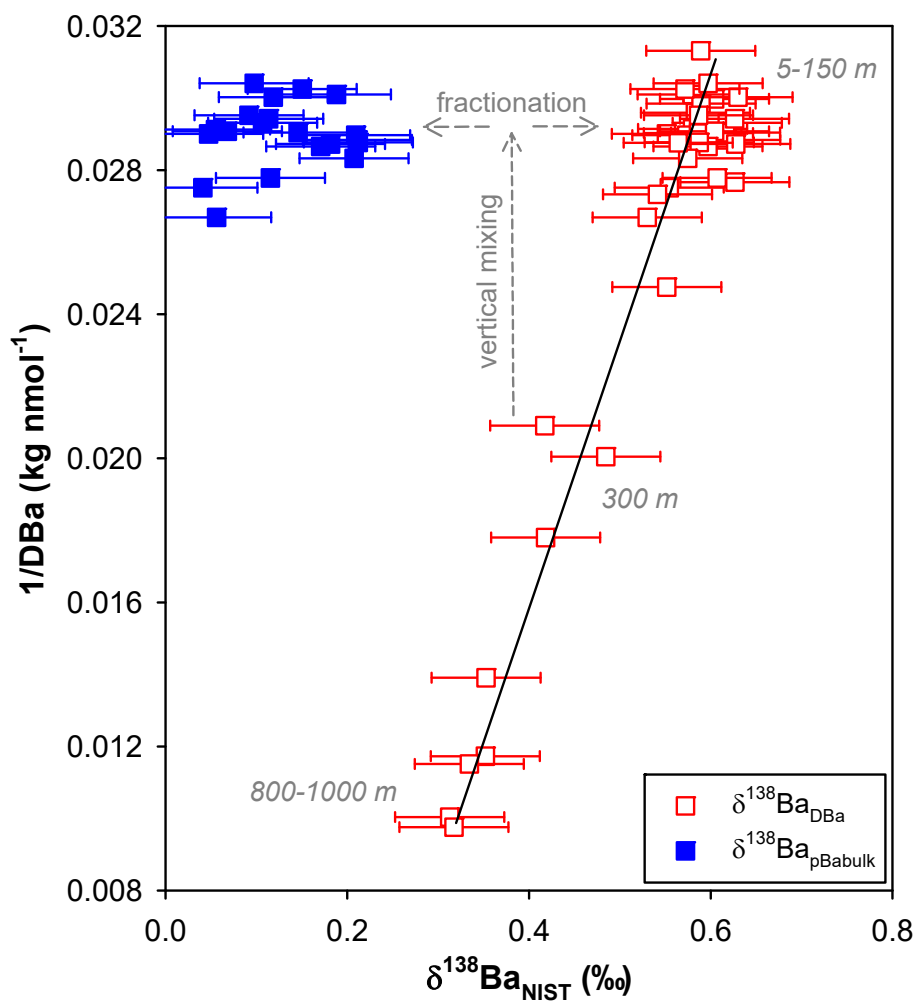
730 **Figure 4.** Vertical distributions of (a) dissolved barium (DBa) and (b) their stable barium isotopic compositions
731 ($\delta^{138}\text{Ba}_{\text{DBa}}$) in the upper 1000 m of the water column at stations A1, A10, and S504 in the northern South China
732 Sea.



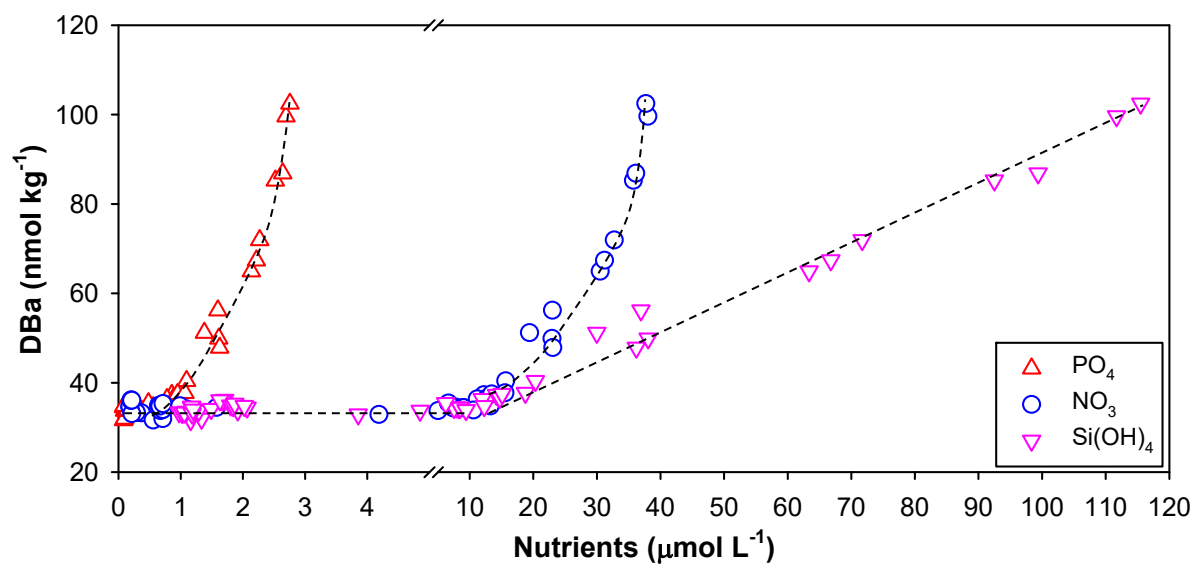
734 **Figure 5.** Vertical distributions of excess particulate barium (pBa_{xs}), particulate aluminum and calcium (pAl
 735 and pCa), particulate organic carbon and nitrogen (POC and PON), biogenic silica (BSi), and chlorophyll a
 736 (Chl-a) in the upper 150 m of the northern South China Sea. (a-d) station A5; (e-h) station A2; (i-l) station A1;
 737 (m-p) station A10; (q-t) station S504. Data of POC and PON and Chl-a were previously published in Cai et al.
 738 (2015) and Chen et al. (2015).



740 **Figure 6.** $1/\text{DBa}$ versus $\delta^{138}\text{Ba}_{\text{DBa}}$ and $\delta^{138}\text{Ba}_{\text{pBabulk}}$ for samples collected in the northern South China Sea. The
741 solid line indicates the vertical mixing throughout the water column, while the numbers in italics indicate the
742 sampling depth/depth range of distinct data point clusters along the line. The dashed arrows denote the Ba
743 isotope fractionation in the upper 150 m based on DBa supply from deep waters via vertical mixing.



745 **Figure 7.** DBa versus nutrients for samples collected in the upper 1000 m of the water column in the northern
746 South China Sea. The dashed lines indicate the various trends of DBa-PO₄, DBa-NO₃, and DBa-Si(OH)₄
747 relationships. Nutrient data were previously published in Cao et al. (2012), Dai et al. (2013), and Du et al.
748 (2013).



750 **Figure 8.** Particulate matter versus Chl-a for samples collected in the upper 150 m of the northern South China
751 Sea. (a) pBa_{xs} and pCa ; (b) POC, PON, and BSi. Data of POC and PON and Chl-a were previously published in
752 Cai et al. (2015) and Chen et al. (2015).

